Brain asymmetries from mid- to late life and hemispheric brain age

Max Korbmacher[1,2,3*], Dennis van der Meer[2,4], Dani Beck[2,5,6], Ann-Marie de Lange[2,7,8], Eli Eikefjord[1,3], Arvid Lundervold[1,3,9,10], Ole A. Andreassen[2,11], Lars T. Westlye[2,6,11], Ivan I. Maximov[1,2*]

[1]Department of Health and Functioning, Western Norway University of Applied Sciences, Bergen, Norway.
[2]NORMENT Centre for Psychosis Research, Division of Mental Health and Addiction, University of Oslo and Oslo University Hospital, Oslo, Norway.
[3]Mohn Medical Imaging and Visualization Centre (MMIV), Bergen, Norway.
[8]Department of Psychiatry, University of Oxford, Oxford, UK.
[7]LREN, Centre for Research in Neurosciences - Department of Clinical Neurosciences, CHUV and University of Lausanne, Lausanne, Switzerland.
[4]Faculty of Health, Medicine and Life Sciences, Maastricht University, Maastricht, Netherlands.
[5]Department of Psychiatric Research, Diakonhjemmet Hospital, Oslo, Norway.
[6]Department of Psychology, University of Oslo, Oslo, Norway.
[9]Department of Radiology, Haukeland University Hospital, Bergen, Norway.
[10]Department of Biomedicine, University of Bergen, Bergen, Norway.
[11]KG Jebsen Centre for Neurodevelopmental Disorders, University of Oslo, Oslo, Norway.

*Corresponding authors. E-mails: max.korbmacher@hvl.no; ivan.maximov@hvl.no;

ABSTRACT

The human brain demonstrates structural and functional asymmetries which have implications for ageing and mental and neurological disease development. We used a set of magnetic resonance imaging (MRI) metrics derived from structural and diffusion MRI data in N=48,040 UK Biobank participants to evaluate age-related differences in brain asymmetry. Most regional grey and white matter metrics presented asymmetry, which were higher later in life. Informed by these results, we conducted *hemispheric brain age* (HBA) predictions from left/right multimodal MRI metrics. HBA was concordant to conventional brain age predictions, using metrics from both hemispheres, but offers a supplemental general marker of brain asymmetry when setting left/right HBA into relationship with each other. In contrast to WM brain asymmetries, left/right discrepancies in HBA are lower at higher ages. Our findings outline various sex-specific differences, particularly important for brain age estimates, and the value of further investigating the role of brain asymmetries in brain ageing and disease development.

INTRODUCTION

There are various structural and functional differences in brain architecture between the left and right hemispheres[1–6]. Microstructural brain characteristics, such as white matter (WM) pathways or intra- and extra-neurite water organisation, might underlie the brain's functional lateralisation[7]. Functional network difference has been associated with handedness[8]. Both structural and functional brain asymmetry exhibit clinical importance as there are differences in brain asymmetry between healthy controls and various disease groups, including neurodegenerative diseases such as Alzheimer's disease[9, 10], Parkinson's disease[11], and psychiatric disease such as obsessive–compulsive disorder[4, 12, 13] and schizophrenia[14]. In that context and particularly relevant from a lifespan-perspective, cortical thickness asymmetry decreases throughout ageing, with this alteration being potentially accelerated in the development of neurodegenerative disorders such as Alzheimer's Disease[9]. Similarly, some studies suggest lower WM microstructure asymmetry at higher ages, indicated by intra-axonal water fraction[15], fractional anisotropy, or the apparent diffusion coefficient[16]. Additional investigations into brain asymmetries' age-dependencies can provide a more comprehensive understanding of the influence of asymmetries on ageing and disease development.

Brain age is a developing integrative marker of brain health, particularly sensitive to neurodegenerative diseases[17, 18]. Brain age refers to the predicted age in contrast to chronological age and is based on a set of scalar metrics derived from brain scans such as MR. To date, brain age has often been estimated using a global brain parametrisation such as the averaged scalar measures over particular anatomical regions or the whole brain[17–21]. Hence, we refer to these whole-brain age predictions as global brain age (GBA). However, while brain age has been calculated for different brain regions[18, 22–24], the use of hemisphere-specific data is usually not being considered as a potential source of additional information. Yet, one study presents hemisphere-specific

and region-specific brain ages containing useful clinical information about post-stroke cognitive improvement[22].

Previous results show that brain age prediction depends on the specific features used[25–27], rendering for example modality as important. Yet, the influence of hemispheric differences or brain asymmetry on the age predictions remains unclear. However, previously outlined brain asymmetries[1–6] might be informative for age predictions. One way of leveraging brain asymmetries into simple metrics is to estimate separate brain ages for each hemisphere (HBA) and to then compare the estimates. It remains unclear whether predictions from a single hemisphere lead to less accurate predictions due to the inclusion of less data and a potential attenuation of noise. At the same time, in the case of diffusion MRI (dMRI), different model-based diffusion features yield highly concordant brain age predictions, also when varying the number of included features[21]. Finally, although the evidence is mixed on the influence of handedness on brain asymmetry[28–31], differences in handedness are potentially reflected in brain structure, which would in turn influence age predictions differently when obtained from the left or right hemisphere only. Hence, handedness requires further examination as potential confounding effect when assessing asymmetry.

HBA, a new brain age measure, may propose more sensitive brain health markers than GBA, as age predictions can be compared between hemispheres to infer the integrity of each hemisphere and give a general estimate of brain asymmetry. Brain asymmetries are commonly observed using the Laterality Index (LI)[32]. However, different ways of estimating asymmetry can introduce variability in its dependency with age[33], and covariates of brain age require further investigation[34, 35]. To extend the existing brain age conceptualisation of using features across the whole brain and to maximise interpretability, we restrict brain age predictions to region-averaged and global features and not asymmetries of these features. Additionally, differences in the models' abilities to predict age from WM microstructure features derived from dMRI compared to T_1-weighted features (volume, surface area, thickness) need to be ruled out in order to validate both GBA and HBA.

Hence, in the present work, we tested first the preregistered hypotheses (written study and analysis plan prior data inspection and analyses[36, 37]) that the GBA and HBA depend on the used MRI modality (Hypothesis 1), disentangling whether the different grey matter (GM) and WM metrics and the degree of their asymmetry influences brain age predictions. We furthermore tested whether there was an effect of hemisphere (Hypothesis 2) and handedness (Hypothesis 3) on brain age predictions. Exploratory analyses included (a) revealing hemispheric differences between GM and WM features, (b) examining LI associations with age, including the LI of the brain features as well as left and right brain ages, and (c) testing the consistency of brain age-covariate associations (specifically, health-and-lifestyle factors, as these were previously associated with brain age[20, 26, 38–41]).

RESULTS

Hemispheric differences and age sensitivity for GM and WM features

Two-tailed paired samples t-tests showed that a significant proportion of the GM and WM features differed between hemispheres with medium effect sizes. Among the significant 793 of 840 dMRI feature asymmetries (94.4%, $p<.05$, with Cohen's $|\bar{d}_{dMRI}| = 0.57\pm0.44$). The largest differences were found for DTI FA in the inferior longitudinal fasciculus ($d = 3.64$), and cingulum ($d = 1.95$), and for AD in superior longitudinal fasciculus.

Effects sizes of the significant hemispheric differences of the 115 of 117 T_1-weighted features (98.3%), were similar: mean $|\bar{d}_{T_1}| = 0.53\pm0.41$, and the largest asymmetries were found for the surface area of the transverse-temporal region ($d = 1.81$), frontal pole ($d = 1.76$), and pars orbitalis ($d = 1.74$; see Supplementary Table 10 for T_1-weighted and dMRI features with strongest hemispheric differences).

Likelihood Ratio Tests (LRTs) comparing a baseline model predicting age from sex and scanner site compared to a model where the respective smooth of the metric was added (Eq. 3 and 4) indicated most features as age-sensitive (231 of the 234 (98.72%) of the T_1-weighted features; 1601 of the 1680 (95.53%) dMRI features). Age-sensitivity was strongly expressed in both significant T_1-weighted features ($\bar{F}_{T_1} = 1{,}168.90\pm993.59$), as well as significant dMRI metrics ($\bar{F}_{dMRI} = 1{,}208.97\pm943.52$) with strongest age-sensitivity observed for left superior temporal thickness, left/right overall thickness, left/right hippocampus volume, and right inferior parietal thickness and multiple WMM metrics in the right anterior limb of the internal capsule, the left-/right fornix-striaterminalis pathway, left/right anterior corona radiata and inferior fronto-occipital fasciculus ($F > 3{,}000$; for top features see Supplementary Table 2). Results were similar when comparing linear models to the baseline model (Eq. 2 and 4): 1448 of the 1680 (86.19%) dMRI metrics, and 228 of the 234 (97.44%) of the T_1-weighted features were age-sensitive ($\bar{F}_{T_1} = 3{,}426.89\pm2{,}947.11$, $\bar{F}_{dMRI} = 2{,}378.46\pm2{,}357.80$), with the features with the strongest age-sensitivity resembling LRT results of non-linear models (for top features see Supplementary Table 3).

Considering only left/right averages identified only DTI-AD, and WMTI axial and radial extra-axonal diffusivity to not differ between hemispheres ($p > .05$). Furthermore, all features were age-sensitive when GAMs ($p < 3.4 \times 10^{-64}$; yet for linear models, BRIA-vCSF and WMTI-axEAD, as well as right DTI-AD and left WMTI-radEAD were not age sensitive (Supplementary Tables 4, 5). Furthermore, the age-relationships for most of the left/right averages were similar across hemispheres (Figure 1, both for crude and adjusted values: Supplementary Figure 1, and for linear and non-linear models: Supplementary Figure 4). However, differences in dMRI metrics were observed for the ends of the distribution including individuals aged younger than 55 ($N = 5{,}307$) and older than 75 ($N = 3{,}480$).

GM and WM feature asymmetry

Using LRTs comparing GAMs to a baseline model 53 (45.30%) of the 117 T_1-weighted and 733 of the 840 (87.26%) dMRI $|LI|$ features as age sensitive (p<.05). Using LRTs on linear effects identified 53 (45.30%) of the 117 T_1-weighted and 678 of the 840 (80.71%) dMRI $|LI|$ features as age sensitive (p<.05).

In the following we constrain analyses to linear models and present partial derivatives / slopes as a measure of effect size, allowing for simple comparisons across age-relationships as model fit indices AIC and BIC of linear models and GAMs suggested on average no differences across both T_1-weighted ($p_{adj\ AIC} = .759$; $p_{adj\ BIC} = 1$) and diffusion-weighted features ($d_{AIC} = 0.510, p_{adj\ AIC} = .020$; $p_{adj\ BIC} = .126$).

The absolute feature asymmetries were higher later in life ($\bar{\beta}_{dMRI} = 0.05 \pm 0.07$; $\bar{\beta}_{T_1} = 0.03 \pm 0.06$, $|\bar{\beta}_{multimodal}| = 0.05 \pm 0.07$, here only $p_{adj} < .05$ selected; Supplementary Figure 2-3).

The strongest adjusted relationships between the respective features' asymmetries and age were found for dMRI metrics ($|\bar{\beta}_{dMRI}| = 0.08 \pm 0.05$, $|\bar{\beta}_{T_1}| = 0.05 \pm 0.03$; Figure 2), particularly outlining asymmetry increases in the cingulate gyrus ($\beta_{BRIA-microRD} = 0.25$, $\beta_{BRIA-microFA} = 0.22$, $\beta_{DTI-MD} = 0.20$, $\beta_{BRIA-microADC} = 0.19$), and decrease in the cerebral peduncle ($\beta_{SMTmc-extratrans}$ = -0.20, $\beta_{SMT-trans}$ = -0.19, $\beta_{BRIA-Vextra}$ = -0.14) and superior longitudinal temporal fasciculus ($\beta_{BRIA-microAX}$ = -0.17, $\beta_{SMT-long}$ = -0.17, $\beta_{BRIA-DAXextra}$ = -0.16).

For T_1-weighted metrics, larger structures' $|LI|$ were most sensitive to age, with the strongest negative associations including the inferior lateral (β = -0.16) and lateral ventricles (β = -0.09), pallidum (β = -0.11) volumes, rostro-middle thickness (β = -0.11), thalamus volume (β = -0.07) and enthorinal area (β = -0.05). Largest positive age-associations were were shown for accumbens area ($\beta = 0.13$), WM surface area ($\beta = 0.13$) and volume ($\beta = 0.11$), amygdala ($\beta = 0.11$), caudal anterior cingulate thicknes ($\beta = 0.11$), cortex volume ($\beta = 0.10$), caudate volume ($\beta = 0.10$), and cerebellar WM volume ($\beta = 0.09$), in addition to several temporal and limbic areas (Figure 2).

Sex-specific differences in the influence of hemisphere, modality, and handedness on brain age estimates

Model performance metrics indicated that most accurately age predictions were accomplished using multimodal MRI data based on left, right, and both hemispheres (Table 1), with obtained HBA and GBA being strongly correlated with each other for similar models (Figure 3). Additional sex-stratified models produced similar results in terms of model performance (Supplementary Table 14), associations across brain ages and age (Supplementary Figure 10), and feature importance rankings (compare Supplementary Tables 11, 12, and 13).

LMERs did not indicate a difference between modalities (Hypothesis 1) when comparing brain ages estimated from both sexes from dMRI to multimodal MRI ($p = .623$), and dMRI to T_1-weighted MRI ($p = .452$). There were also no differences in brain age estimates between hemispheres ($p = .413$, Hypothesis 2). Moreover, LRTs indicated no significant difference between models when adding handedness

($\chi^2 = 4.19$, $p = .123$, $df = 2$) or handedness-hemisphere interaction and handedness ($\chi^2 = 7.32$, $p = .120$, $df = 4$; see Eqs. 5-6).

To additionally consider sex differences, we estimated additional sex-specific brain ages and control for the modelling choice (as extension to Eq. 6). We find that females' brain ages do not differ when estimated from females' data only compared to predictions from both males' and females' data ($\beta = -0.0073\ years, p = .420$). The same holds true for male brain ages estimated from males' data only compared to data from both sexes ($\beta = -0.0002\ years, p = .984$). Furthermore, with these additional modelling choices, we identified a significant marginal effect of sex (indicating an older brain age for males: $\beta = 0.58\ years, p < .001$), and hemisphere for T_1-weighted ($\beta = 0.03\ years, p = .022$), but not dMRI ($\beta = 0.02\ years, p = .099$), or multimodal MRI ($\beta = 0.02\ years, p = .110$). Moreover, ambidextrous brain age was higher than for left-handed ($\beta = 1\ year, p < .001$) and right handed participants ($\beta = 0.7\ years, p < .001$), as well as higher for right-handed compared to left-handed participants ($\beta = 0.2\ years, p < .001$).

Further investigating the identified sex-effect, we found higher brain ages for males across modalities with larger differences identified for dMRI ($\beta_{left} = 0.768\ years, p < .001$, $\beta_{right} = 0.870\ years, p < .001$), followed by T_1-weighted ($\beta_{left} = 0.308\ years, p < .001$, $\beta_{right} = 0.438\ years, p < .001$) and multimodal MRI ($\beta_{left} = 0.503\ years, p < .001$, $\beta_{right} = 0.570\ years, p < .001$). Notably, females' right brain age was lower than the left brain age ($\beta_{T_1} = -0.035\ years, p = .027$, $\beta_{dMRI} = -0.029\ years, p = .066$, $\beta_{multimodal} = -0.013\ years, p = .403$), which was the opposite for males showing lower left brain age ($\beta_{T_1} = 0.095\ years, p < .001$, $\beta_{dMRI} = 0.073\ years, p < .001$, $\beta_{multimodal} = -0.054\ years, p = .001$). In contrast to the analyses across sexes, these additional analyses provide support for Hypotheses 1-3 when sex-stratifying.

Lower brain age asymmetry at higher ages

To test whether asymmetries between hemisphere-specific brain age predictions are lower at higher age, $|LI_{HBA}|$, was associated with age (Eq. 7-8). $|LI_{HBA}|$ showed negative unadjusted associations with age for T_1-weighted ($r = -0.069$, $p < .001$), dMRI ($r = -0.121$, $p < .001$), and multimodal models ($r = -0.121$, $p < .001$). The associations were similar when using LMEs adjusting for sex and the random intercept site (T_1-weighted: $\beta = -0.069$, $p < .001$, dMRI: $\beta = -0.115$, $p < .001$, multimodal: $\beta = -0.117, p < .001$). LRTs indicate the age-sensitivity of LI_{HBA} (T_1-weighted: $\chi^2 = 173.42$, $p < .001$, dMRI: $\chi^2 = 488.74$, $p < .001$, multimodal: $\chi^2 = 506.08$, $p < .001$).

These results were robust to stratifying by sex, estimates from a brain age model considering both sexes for unadjusted ($r_{dMRI\ males} = -0.134$, $r_{dMRI\ females} = -0.104$,$r_{T1\ males} = -0.134$, $r_{T1\ females} = -0.048$, $r_{multimodal\ males} = -0.134$, $r_{multimodal\ females} = -0.111$), and adjusted associations ($\beta_{dMRI\ males} = -0.134$, $\beta_{dMRI\ females} = -0.099$, $\beta_{T1\ males} = -0.134$, $\beta_{T1\ females} = -0.045$, $\beta_{multimodal\ males} = -0.134$, $\beta_{multimodal\ females} = -0.106$), with χ^2 tests suggesting age sensitivity (all $p < .001$).

Using brain age predictions from models which were independently estimated for males and females showed similar results for unadjusted ($r_{dMRI\ males} = -0.141$, $r_{dMRI\ females} = -0.094$,$r_{T1\ males} = -0.120$, $r_{T1\ females} = -0.031$, $r_{multimodal\ males} = -0.165$, $r_{multimodal\ females} = -0.089$), and adjusted associations ($\beta_{dMRI\ males} = -0.137$, $\beta_{dMRI\ females} = -0.088$, $\beta_{T1\ males} = -0.117$, $\beta_{T1\ females} = -0.029$, $\beta_{multimodal\ males} = -0.162$, $\beta_{multimodal\ females} = -0.084$), with χ^2 tests suggesting age sensitivity (all $p < .001$).

Finally, also when analysing brain ages for males and females from sex-specific models together shows similar trends for uncorrected $|LI_{HBA}|$-age associations ($r_{multimodal} = -0.123$, $p < .001$; $r_{T_1} = -0.074$, $p < .001$, $r_{dMRI} = -0.114$, $p < .001$), as well as corrected association ($\beta_{multimodal} = -0.125$, $p < .001$; $\beta_{T_1} = -0.071$, $p < .001$, $\beta_{dMRI} = -0.113$, $p < .001$; Eq. 7-8).

HBA and GBA and health-and-lifestyle factors

We further investigated the pattern of relationships with general health-and-lifestyle phenotypes across HBAs (Figure 4). Relationships between brain ages from single and both hemispheres were similar within modalities, but varied slightly between modalities (Figure 4). These results were robust to sex stratifications. Yet, while males' brain age was sensitive to high cholesterol, hip circumference, smoking and weight, this was not the case for females' brain age when using brain age predictions from data of both sexes (Supplementary Figure 11-12).

Sex stratified hemispheric differences and age sensitivity for GM and WM features

For further insights into sex differences, we repeated the presented analyses on hemispheric differences and features' age-sensitivity stratifying by sex. Two-tailed paired samples t-tests assessing regional differences between hemispheres showed similar results between sexes, which are also comparable to cross-sex results. Most features differed between hemispheres for both males and females (T_1-weighted: 98.3% for both sexes, $dMRI_{males}$: 96%, $dMRI_{females}$: 95%), and effect sizes were similar ($|\bar{d}_{T_1 males}| = 0.54 \pm 0.42$, $|\bar{d}_{T_1 females}| = 0.53 \pm 0.42$, $|\bar{d}_{dMRI\ males}| = 0.57 \pm 0.41$, $|\bar{d}_{dMRI\ females}| = 0.60 \pm 0.47$).

Also the strongest effects were similar across sexes: strongest differences in T_1-weighted features in males were observed for frontal pole ($d_{T_1 males} = 1.82$) and pars orbitalis ($d_{T_1 males} = 1.78$) surface area, and for females in the area of the transverse temporal area ($d_{T_1 females} = 1.89$) and the frontal pole ($d_{T_1 females} = 1.73$). Strongest WM differences were observed for both sexes in inferior longitudinal fasciculus ($d_{dMRI\ males} = 3.44$, $d_{dMRI\ females} = 3.91$), and superior lonitudinal temporal fasciculus ($d_{dMRI\ males} = 2.09$, $d_{dMRI\ females} = 2.40$; Supplementary Table 6).

LRTs comparing a baseline model predicting age from sex and scanner site compared to a model where the respective smooth of the metric was added (Eq. 3 and 4) indicated most features as age-sensitive (230 of the 234 (98.29%) of the T_1-weighted features (both sexes); 1,557 and 1564 of the 1,680 (92.68% and 93.10%) dMRI features for males and females, respective). Age-sensitivity was strongly expressed in both

significant T_1-weighted features ($\bar{F}_{T_1 males} = 640.80 \pm 521.33$; $\bar{F}_{T_1 females} = 578.61 \pm 500.79$), as well as significant dMRI metrics ($\bar{F}_{dMRI\ males} = 586.38 \pm 450.68$, $\bar{F}_{dMRI\ females} = 674.61 \pm 499.58$).

Similar to the results including both sexes, the strongest T_1-weighted feature age-sensitivity was observed for left superior temporal thickness, left/right hippocampus volume for both sexes, and right inferior parietal thickness only for females. Concerning dMRI features, sex stratification reflects the findings accounting for sex, outlining the fornix-striaterminalis pathway, anterior corona radiata and inferior fronto-occipital fasciculus, yet adding the anterior limb of the internal capsule and the anterior thalamic radiation. Unique to non-linear models, also the lateral ventricle volume was lined out as highly age sensitive (all $F > 1,666$; for top features see Supplementary Table 7.

Results were similar when comparing linear models to the baseline model (Eq. 2 and 4): 1,557 and 1,564 of the 1680 (92.68%, 93.01%) dMRI metrics, and 226 and 224 of the 234 (96.58%, 95.73%) of the T_1-weighted features were age-sensitive for males and females, respectively ($\bar{F}_{T_1 males} = 1{,}767.60 \pm 1{,}474.69$; $\bar{F}_{T_1 females} = 1{,}712.73 \pm 1{,}488.97$; $\bar{F}_{dMRI\ males} = 1{,}198.85 \pm 1{,}135.84$, $\bar{F}_{dMRI\ females} = 1{,}297.51 \pm 1{,}257.02$), with the features with the strongest age-sensitivity resembling LRT results of non-linear models (for top features see Supplementary Table 8).

Considering only left and right hemispheric averages, t-tests indicated that all features differed between hemispheres for males ($p < 3.1 \times 10^{-9}$). In females, WMTI radEAD and axEAD as well as DTI AD did not differ between hemispheres ($p > 0.05$), but all other metrics differing between hemispheres ($p < 1.5 \times 10^{-36}$).

Considering all regional features, LRTs on GAMs (Eq. 4, 3) indicated that all features were age-sensitive ($p < 5.1 \times 10^{-71}$). LRTs on linear models (Eq. 2, 4) indicated that right hemisphere BRIA-vCSF and left microRD were not age sensitive ($p_{adj} > 0.05$) in males. In females, additionally, left DTI-RD and GM thickness as well as left and right WMTI-axEAD were not age-sensitive. All other metrics were age sensitive ($p < 2.7 \times 10^{-11}$). Hemispheric features' age-relationships showed similar intercepts and slopes across sexes, except DTI-AD, WMTI-radEAD and WMTI-axEAD (Supplementary Figure 5-6).

Sex differences in GM and WM feature asymmetry

Sex-stratified analyses indicate most dMRI $|LI|$ features to be age sensitive ($\text{dMRI}_{males} = 64.29\%$, $\text{dMRI}_{females} = 69.52\%$), but less T_1-weighted features ($\text{T}_{1\ males} = 47.86\%$, $\text{T}_{1\ females} = 38.46\%$) when using non-linear models. Linear models showed similar results ($\text{dMRI}_{males} = 60.95\%$, $\text{dMRI}_{females} = 64.05\%$; $\text{T}_{1\ males} = 44.44\%$, $\text{T}_{1\ females} = 37.61\%$). Comparing linear to non-linear models using paired samples t-tests suggests no differences model fit indicated in AIC or BIC scores for both males and females in T_1-weighted and diffusion features' asymmetry ($p > 0.05$). Hence, linear model outcomes are presented below. Similar to models including both sexes, when stratifying for sex, $|LI|$ for diffusion and T_1-weighted feature were positively associated with age ($\bar{\beta}_{dMRI\ male} = 0.05 \pm 0.08$, $\bar{\beta}_{dMRI\ female} = 0.05 \pm 0.08$, $\bar{\beta}_{T1\ male} = 0.03 \pm 0.06$, $\bar{\beta}_{T1\ female} = 0.03 \pm 0.06$).

The strongest adjusted relationships for diffusion features were found in the cingulate gyrus tract ($\beta_{males\ BRIA-microRD} = 0.25$, $\beta_{males\ BRIA-microFA} =$

0.22, $\beta_{females\ BRIA-microRD} = 0.25$, $\beta_{males\ BRIA-microFA} = 0.21$) and in the cerebral peduncle ($\beta_{males\ SMTmc-extratrans} = -0.19$, $\beta_{males\ SMT-trans} = -0.18$, $\beta_{females\ SMTmc-extratrans} = -0.21$, $\beta_{females\ SMT-trans} = -0.20$, $\beta_{females\ BRIA-Vextra} = -0.18$; Supplementary Figures 8, 9). Strongest age associations with T_1-weighted asymmetries were found for the area of the accumbens ($\beta_{males} = 0.14, \beta_{females} = 0.12$) and WM surface ($\beta_{males} = 0.13, \beta_{females} = 0.12$), with strongest inverse relationships observed for inferior lateral ventricles ($\beta_{males} = -0.17$, $\beta_{females} = -0.14$) and pallidum ($\beta_{males} = -0.11$, $\beta_{females} = -0.12$).

DISCUSSION

In the present work we investigated a new way of utilising brain age to differentiate between hemispheres, and performed a detailed assessment of brain asymmetry associations with age. As a baseline, we showed that most grey and white matter features were age-sensitive and differed between hemispheres with relatively large effect sizes. Brain asymmetry was age-sensitive, and overall higher at higher ages. In contrast, asymmetry in hemispheric brain age was lower at higher ages. The strongest relationship of age and absolute brain asymmetry was identified in larger GM and WM regions, as well subcortical structures, including the limbic system, the ventricles, cingulate and cerebral as well as cerebellar peduncle WM.

Brain age predictions exhibited concordant accuracy within modalities for left, right, and both hemispheres, and concordant associations with health-and-lifestyle factors also when analysing data for males and females separately, training brain age models on data from each sex separately or both sexes together. The predictions did not differ statistically between hemispheres, modalities, or handedness groups when considering both sexes together. However, sex-stratified analyses, which considered different brain age modelling choice, revealed significant opposing effects between sexes for hemisphere and modality, and outlined marginal differences between handedness groups. There are multiple reasons for the observed higher brain age in females' right hemisphere compared to males' higher brain age of the left hemisphere, in addition to modality-specific differences. First, male and female brain structure differs, resulting in sex-specific regional variations in brain age estimates[42]. Second, body and brain ageing trajectories differ between sexes, for example, outlined by sex-dependent importance of cardiometabolic risk factors[43] . Hence, the tendency of males' predicted brain age being lower using T_1-weighted and multimodal in contrast to diffusion-derived brain ages, with these trends reversed in females, might also reflect stronger brain age associations with cardiometabolic risk factors in males (Supplementary Figure 7), which have been demonstrated earlier for WM features and WM brain age[38, 39]. HBA allows to assess the structural integrity of each hemisphere individually, and to set brain ages from the two hemispheres in relationship to each other providing a general marker of asymmetry. Despite brain asymmetries overall increasing (Supplementary Figures 2-3), the asymmetries between left/right HBA were smaller at a higher age. At higher ages, both hemispheres might hence become overall more comparable, despite ageing-related changes[44].

We found that the majority of regional and hemisphere-averaged MRI features differed between hemispheres. Both features and asymmetries were age-sensitive indicating that the investigation of asymmetries are useful across ages and MRI modalities.

Interestingly, hemisphere-averaged features' age-associations and HBA of the same modality were similar between hemispheres (Figure 1), and the hemisphere was not a significant predictor of brain age estimated from a particular hemisphere, when analysing data from both sexes together. However, when sex-stratifying, modality and hemisphere were significant predictors, suggesting that HBA captures both brain asymmetries as well as biological sex-differences which become apparent when using multimodal MRI. These results outline the importance of considering sex-differences in brain age analyses.

Several studies present evidence for asymmetries in WM[6, 45–48] and GM[4, 9, 49–51]. In contrast to these previous studies, for the first time, we examine various metrics supplying information on both WM and GM in a large sample. While we find various differences between hemispheres, age relationships of T_1-weighted and dMRI features were similar between hemispheres using hemispheric averages, also when stratifying by sex. Spatially finer-grained examinations revealed more specific patterns of asymmetry in T_1-weighted features, such as GM thickness[9], and dMRI features[45]. This is also shown in the present study by stronger age-effects for specific regional asymmetries compared to asymmetries in hemispheric averages. Age-MRI metric relationships depend, however, on the selected metric, the sample, and the sampling (cross-sectional or longitudinal)[52, 53]. For example, previous evidence from T_1-weighted MRI indicates no differences in GM volume between hemispheres[54], but hemispheric differences of cortical thickness and surface area across ageing[4, 9].

The presented age charts of MRI metrics in the current work (Figure 1, Supplementary Figure 1) provide similar trends to those reported in previous studies observing global age dependencies[19, 21, 55–57]. Yet, the stratification between hemispheres when presenting brain features' age dependence is a novel way of presenting brain charts.

We found asymmetries based on GM and WM brain scalar measures. Unimodal studies with smaller, younger samples presented age-dependence of the brain asymmetry during early WM development[48] and adult cortical thickness[9], other T_1-derived metrics[33], and functional network development[5], showing lower asymmetry at higher ages. In contrast to HBA asymmetries, brain asymmetries do generally not support the notion of lower but instead of higher brain asymmetry later in life. Different study design choices, such as temporal and spatial levels might provide supplemental information into the age-dependence of brain asymmetries, for example, by further investigating longitudinal and voxel-level asymmetries.

We extended previous findings by providing a comprehensive overview of brain asymmetry associations throughout mid- to late life including both GM and WM. Our findings indicate that when considering various metrics, older brains generally appear less symmetric than younger brains in the current sample mid- to late life sample, whereas brain age appears more symmetric in older brains.

Notably, we identified strong associations between specific brain regions' asymmetry and age. The strongest age-associations of asymmetries were observed for subcortical, ventricle-near structures. The general age-sensitivity of such structures[21, 58, 59] might be a reason for the observed age-associations in asymmetries, and hence pointing towards one hemisphere being stronger affected by degradation effects, or even the involvement of such regions in psychiatric and neurodegenerative disorders[40, 55, 58, 60–65]. For example, the hippocampus, a prominent limbic structure, presents relatively high levels of adult neurogenesis, which might potentially explain repeated findings of the region's associations with psychiatric disorders and disorder states such as depression, anxiety, schizophrenia, addiction, and psychosis[66, 67], and neurdegenerative disorders, especially Alzheimer's Disease[68], but also ageing in general[69]. Some of the strongest age-relationship for T_1-derived asymmetries were observed in the accumbens, ventricles and pallidum. In turn, a series of dMRI approaches was sensitive to asymmetry in the cingulum tract, which is higher in late-life and cerebral peduncle asymmetry which appears lower in late-life. In particular, radial diffusivity metrics, such SMT-trans, SMTmc-extratrans, and BRIA-microRd, and fractional anisotropy indicated by BRIA-microFA were sensitive to age-dependencies of these asymmetries. Although speculative, this observation could indicate a relationship between asymmetry and axonal properties during ageing, such as myelination, density, or diameter, in the cingulum, with yet a more general marker (BRIA-microFA) of anisotropy asymmetry increasing at advanced age. However, limitations of the different diffusion metrics, such as the inability to account for axonal swelling, infection, or crossing fibres[70], aggravates the interpretation of such asymmetry changes. Overall, asymmetries' age-dependencies in subcortical, limbic and ventricle-near areas are not surprising, considering that the cingulum and cerebral peduncle WM, and middle temporal GM area also presented some of the strongest asymmetries across the sample (Supplementary Table 10).

Both GM volume, surface, and thickness show asymmetries across studies[1, 3, 4, 9, 54]. We identified lower asymmetry linked to higher ages in the ventricular and pallidum volumes, appearing alongside the known effect of larger ventricle volumes at higher ages[55]. The strongest positive age-relationships for T_1-weighted features' asymmetry were observed for accumbens and WM surface area, as well as limbic structures such as amygdala, hippocampus, and cingulate. Limbic structures have previously been outlined as highly age-sensitive[21, 58, 59, 69]. Higher asymmetry-levels might speak to asymmetric atrophy in these limbic regions, potentially explaining several ageing-related effects[9]. However, lifespan changes in ventricular volume asymmetry in relation to symptom and disorder expression requires additional investigations.

Cingulum WM microstructure has been reported to differ between hemispheres[71–73]. Abnormalities in cingulum asymmetry have been linked to schizophrenia[74–76] and epilepsy[77, 78], and Alzheimer's disease[59]. Additionally, the cingulum tract was associated with the anti-depressant effects of deep brain stimulation in treatment-resistant depression[79]. Recent evidence points out strongest polygenic risk associations for several psychiatric disorders in addition to Alzheimer's Disease with longitudinal WM in the cerebral peduncle[58]. Future research could assess

regional asymmetries to evaluate such metrics' value for diagnostics and treatment in a range of brain disorders.

Overall, most absolute MRI feature asymmetries were positively related to age, with brain age asymmetries showing inverse age-relationships. However, for both WM and GM this process was observed to be spatially distributed. Metric-specific changes might indicate accelerated and pathological ageing[9], which urges to examine different WM and GM metrics across temporal and spatial resolutions and in clinical samples.

Informed by the presented brain asymmetries and their age-dependence, we suggest HBA, indicating the structural integrity of each hemisphere when compared to the chronological age. Moreover, HBA provides a general marker of asymmetry, when setting left/right HBA in relationship to each other. While this added information to conventional GBA is promising, first, the degree to which HBA captures GBA predictions, had to be assessed. This investigation included (1) direct comparisons of HBA and GBA models and their predictions, (2) the influence of covariates of brain age including MRI modality, hemisphere, handedness, and the hemisphere-handedness interaction effect, and (3) a comparison of health-and-lifestyle phenotype-associations with HBA and GBA. Overall, HBA and GBA were highly similar across these dimensions, yet different between hemispheres and modalities within males and females, with these differences contrasting each other. This renders HBA sensitive to potential underlying biological processes which only become apparent when assessing males and females separately. Additionally, different modalities might be sensitive to a range of biological phenomena in terms of brain age, such as dMRI brain age which presents group differences for diabetes only in males. In that sense, a further route of investigation could be to establish sex-specific uni- and multimodal brain age models (which account for sex differences in brain morphology and its developmental trajectories). The influence of hemisphere and sex on how these models relate to biological phenomena can then be assessed.

Congruently with previous research which combined MRI modalities[27], we found higher prediction accuracy for multimodal compared to unimodal predictions for both HBA and GBA. Our results extend previous findings on conventional brain age by not only estimating brain age from different MRI modalities, but also for each hemisphere and sex separately. HBA could hold potential in clinical samples by informing about the consistency between the two hemispheres' brain age predictions. Particularly diseases or conditions which affect a single hemisphere, such as unilateral stroke or trauma, might then be sensitively detected, and the integrity of the unaffected hemisphere can be assessed by observing the congruence of HBA[22]. Larger discrepancies between HBAs of the same individual might act as a marker of hemisphere-specific brain health imbalance, which may indicate potential pathology.

While this study provides initial explorations of asymmetries and HBA, our findings remain limited to the examined sample (imaging subset of the UKB), and limited by generational effects within the sample. The UKB contains individuals born in different decades, which influences individual predispositions for brain health through various factors such as the living environment[80] or education[81], representing various potential confounding effects. Additional bias might have been introduced by the sample characteristics and sampling procedure. The UKB consists of nearly exclusively

white UK citizens, limiting the generalisability beyond white Northern Europeans and US Americans in their midlife to late life. The volunteer-based sampling procedure might additionally have introduced bias, reducing generalisability to the UK population[82], with the imaging sample of the UKB showing an additional positive health bias (better physical and mental health) over the rest of the UKB sample[83], rendering this sub-sample as even less representative of the total UK population.

In conclusion, we identified asymmetries throughout the brain from midlife to late-life. These asymmetries appear higher later in life across GM and WM. Opposing, the difference in left/right hemispheric brain age is smaller at higher ages. We furthermore identify various sex-specific differences in brain age and its correlates, as well as regional asymmetries which do not only show age-dependence but which have also been related to various clinical diagnoses. The identified age-relationships of asymmetries provide future opportunities to better understand ageing and disease development.

METHODS

Sample characteristics

We obtained UK Biobank (UKB) data[84], including $N = 48,040$ T_1-weighted datasets, $N = 39,637$ dMRI datasets, resulting in $N = 39,507$ joined/multimodal datasets after exclusions were applied. Participant data were excluded when consent had been withdrawn, an ICD-10 diagnosis from categories F (presence of mental and behavioural disorder), G (disease of the nervous system), I (disease of the circulatory system), or stroke was present, and when datasets were not meeting quality control standards using the YTTRIUM method[85] for dMRI datasets and Euler numbers were larger than 3 standard deviations below the mean for T_1-weighted data[86]. In brief, YTTRIUM[85] converts the dMRI scalar metric into 2D format using a structural similarity[87, 88] extension of each scalar map to their mean image in order to create a 2D distribution of image and diffusion parameters. These quality assessments are based on a 2-step clustering algorithm applied to identify subjects located outside of the main distribution.

Data were collected at four sites, with the T_1-weighted data collected in Cheadle (58.41%), Newcastle (25.97%), Reading (15.48%), and Bristol (0.14%). Of these data, 52.00% were females, and the participants age range was from 44.57 to 83.71, mean $= 64.86 \pm 7.77$, median $= 65.38 \pm 8.79$. DMRI data were available from four sites: Cheadle (57.76%), Newcastle (26.12%), Reading (15.98%), and Bristol (0.14), with 52.19% female, and an age range of 44.57 to 82.75, mean $= 64.63 \pm 7.70$, median $= 65.16 \pm 8.73$. The multimodal sample ($N = 39,507$) was 52.22% female, with an age range of 44.57 to 82.75, mean $= 64.62 \pm 7.70$, median $= 65.15 \pm 8.73$. Information on sex was acquired from the UK central registry at recruitment, but in some cases updated by the participant. Hence the sex variable may contain a mixture of the sex the UK National Health Service (NHS) had recorded for the participant as well as self-reported sex.

MRI acquisition and post-processing

UKB MRI data acquisition procedures are described elsewhere[84, 89, 90]. The raw T_1-weighted and dMRI data were processed accordingly. Namely, the dMRI data passed through an optimised pipeline[85]. The pipeline includes corrections for noise[91], Gibbs ringing[92], susceptibility-induced and motion distortions, and eddy current artifacts[93]. Isotropic 1 mm^3 Gaussian smoothing was carried out using FSL's[94, 95] *fslmaths*. Employing the multi-shell data, Diffusion Tensor Imaging (DTI)[96], Diffusion Kurtosis Imaging (DKI)[97] and White Matter Tract Integrity (WMTI)[98] metrics were estimated using Matlab 2017b code (https://github.com/NYU-DiffusionMRI/DESIGNER). Spherical mean technique (SMT)[99], and multi-compartment spherical mean technique (SMTmc)[100] metrics were estimated using original code (https://github.com/ekaden/smt)[99, 100]. Estimates from the Bayesian Rotational Invariant Approach (BRIA) were evaluated by the original Matlab code (https://bitbucket.org/reisert/baydiff/src/master/)[101].

T_1-weighted images were processed using Freesurfer (version 5.3) [102] automatic *recon-all* pipeline for cortical reconstruction and subcortical segmentation of the T_1-weighted images (http://surfer.nmr.mgh.harvard.edu/fswiki)[103].

In total, we obtained 28 WM metrics from six diffusion approaches (DTI, DKI, WMTI, SMT, SMTmc, BRIA; see for overview in Supplement 9). In order to normalise all metrics, we used Tract-based Spatial Statistics (TBSS)[104], as part of FSL[94, 95]. In brief, initially all brain-extracted[105] fractional anisotropy (FA) images were aligned to MNI space using non-linear transformation (FNIRT)[95]. Following, the mean FA image and related mean FA skeleton were derived. Each diffusion scalar map was projected onto the mean FA skeleton using the TBSS procedure. In order to provide a quantitative description of diffusion metrics we used the John Hopkins University (JHU) atlas[106], and obtained 30 hemisphere-specific WM regions of interest (ROIs) based on a probabilistic WM atlas (JHU)[107] for each of the 28 metrics. For T_1-weighted data, we applied the Desikan-Killiany Atlas[108]. Altogether, 840 dMRI features were derived per individual [28 metrics $\times$ (24 ROIs + 6 tracts)] for each hemisphere, and 117 T_1-weighted features (surface area, volume, thickness for each of the 34 regions; 3 whole-brain gray matter averages, and 2 averages of white matter surface area and volume) for each hemisphere.

Brain Age Predictions

Brain age was predicted using the XGBoost algorithm[109] implemented in Python (v3.7.1). We used six data subsets to predict brain age split in the following manner: 1) right hemisphere T_1-weighted, 2) left hemisphere T_1-weighted, 3) left hemisphere diffusion, 4) right hemisphere diffusion, 5) left hemisphere multimodal, 6) right hemisphere multimodal. We applied nested k-fold cross-validation with 5 outer and 10 inner folds (see Supplementary Table 1 for tuned hyperparameters for models trained on data from both sexes together and Supplementary Table 15 for models trained separately for males and females). We corrected for age-bias and mere age-effects[110, 111]

by including age in the regression equations (Eq. 5) when assessing effects of modality, hemisphere, and handedness on brain age, as well as phenotype associations with brain ages (Eq. 9).

Statistical Analyses

All statistical analyses were carried out using Python (v3.7.1) and R (v4.2.0).

Hemispheric differences and age sensitivity

To give an overview of the extent of brain asymmetry, we assessed the significance of T_1-weighted and dMRI features' asymmetry using two-sided t-tests. The lateralisation or asymmetry of the brain features was estimated as the following: we applied the LI[32] to both regional features and features averaged over each hemisphere (see also[33]).

$$LI = \frac{L - R}{L + R}, \tag{1}$$

where L and R belongs to any left and right scalar metric, respectively. Furthermore, when associating LI with age, we used absolute LI values ($|LI|$) allowing to estimate age-effects on asymmetry irrespective of the direction of the asymmetry (leftwards or rightwards).

We then used linear regression models correcting for sex and scanning site to predict age from all regular and LI features:

$$\hat{Age} = F + Sex + Site, \tag{2}$$

where F is a scalar metric such as, for example, hippocampus volume (derived from T_1-weighted image) or tapetum fractional anisotropy (derived from DTI). The same model setup was used applying generalised additive models (GAM) to model non-linear relationships between F and Age using a smooth s of linked quadratic functions with k = 4 knots and restricted maximum likelihood (REML):

$$\hat{Age} = s(F) + Sex + Site. \tag{3}$$

Likelihood ratio tests (LRTs)[112] were used to assess the age sensitivity of all T_1-weighted and dMRI features and their asymmetry/LI features by comparing the above models with baseline models not including the respective feature:

$$\hat{Age} = Sex + Site. \tag{4}$$

We used the same procedure for region-averaged and hemispheric average metrics for regular and LI features. Hemispheric averages of regular features were then visualised by age, including surface area, volume, thickness for T_1-weighted data, and intra- and extra-axonal water diffusivities as well as for DTI and DKI metrics.

To compare the model fit of non-linear and linear models we used the Akaike information criterion (AIC)[113] and Bayesian information criterion (BIC)[114].

Brain age assessment

We estimated correlations across HBA and GBA to assess their similarities in addition to the model output provided from the prediction procedure. We also correlated age with the LI (see Eq. 1) for the three modalities (dMRI, T_1-weighted, multimodal MRI), and estimated the age sensitivity of the LI as described in (Eqs. 2-4).

As preregistered (https://aspredicted.org/if5yr.pdf), to test the relationships between hemisphere (H), modality (M), and HBA while controlling for age, sex and scanner site, we employed linear mixed effects regression (LMER) models of the following form:

$$\hat{HBA} = H + M + H \times M + Sex + Age + Sex \times Age + (1|Site) + (1|I), \quad (5)$$

where I refers to the random intercept at the level of the individual. Post-hoc group differences were observed for hemisphere, modality and their interaction.

Next, handedness (Ha) was added to the model to observe whether there are model differences between the resulting LMER:

$$\hat{HBA} = Ha + H \times Ha + H + M + H \times M + Sex + Age + Sex \times Age + (1|Site) + (1|I), \quad (6)$$

and the previous model. Models were statistically compared using LRTs[112].

For sex-stratified analyses, we considered brain age estimates both from models using data from both sexes together, as well as models which were trained on females-only or males-only data. The modelling choice (MC) was included as a factor for the sex-stratified brain age analyses in the formula of Eq. 6.

Finally, the LIs (Eq. 1 of left and right brain age predictions for T_1-weighted, diffusion and multimodal MRI (LI_{HBA}, i.e. the asymmetry in brain age predictions) were associated with age, controlling for sex and scanner site as random effect:

$$\hat{Age} = LI_{HBA} + Sex + (1|Site). \quad (7)$$

The LI_{HBA}s' age-sensitivity was then assessed (as for brain features, see Eqs. 2-4), using LRTs comparing the above model with a baseline model excluding LI_{HBA} (Eq. 4):

$$\hat{Age} = Sex + (1|Site). \quad (8)$$

This procedure was also done for each sex individually, also separating between brain age models predictions which were obtained from the data from both sexes compared to a single sex.

Phenotype associations of brain age

In an exploratory analysis step, we assessed association patterns between brain ages and health-and-lifestyle factors which have previously demonstrated an association with brain age[20, 26, 38–41]. This analysis step served to compare phenotype associations across estimated brain ages. The health-and-lifestyle factors included alcohol drinking (binary), height and weight supplementing body mass index (BMI), diabetes diagnosis

(binary), diastolic blood pressure, systolic blood pressure, pulse pressure, hypertension (binary), cholesterol level (binary), and smoking (binary describing current smokers). For this last analysis step, LMERs were used with the following structure:

$$\hat{P} = BA + Sex + Age + Sex \times Age + (1|Site), \tag{9}$$

where BA refers brain age incorporating both GBA and HBA, P is the phenotype.

Furthermore, where applicable, we corrected p-values for multiple testing using Bonferroni correction and an α-level of $p < .05$. We used a high-precision approach to calculate exact p-values utilizing the Multiple Precision Floating-Point Reliable R package[115], and report standardized β-values. Sex and site were entered as independent factorial nominal variables in the applicable regression models, with sex being a binary (0 = female, 1 = male) and scanner site a multinominal (0 = Cheadle, 1 = Newcastle, 2 = Reading, 3 = Bristol). Finally, we repeated the presented statistical analyses stratifying for sex.

DATA AVAILABILITY

All raw data are available from the UKB (www.ukbiobank.ac.uk).

CODE AVAILABILITY

Analysis code is available at https://github.com/MaxKorbmacher/Hemispheric_Brain_Age.

REFERENCES

[1] Nazlee, N., Waiter, G. D. & Sandu, A.-L. Age-associated sex and asymmetry differentiation in hemispheric and lobar cortical ribbon complexity across adulthood: A uk biobank imaging study. *HBM* **44**, 49–65 (2023).

[2] Karolis, V. R., Corbetta, M. & Thiebaut de Schotten, M. The architecture of functional lateralisation and its relationship to callosal connectivity in the human brain. *Nat. Comm.* **10**, 1417 (2019).

[3] Saltoun, K. *et al.* Dissociable brain structural asymmetry patterns reveal unique phenome-wide profiles. *Nat. Hum. Beh.* 1–18 (2022).

[4] Kong, X.-Z. *et al.* Mapping cortical brain asymmetry in 17,141 healthy individuals worldwide via the ENIGMA Consortium. *PNAS* **115**, E5154–E5163 (2018).

[5] Agcaoglu, O., Miller, R., Mayer, A. R., Hugdahl, K. & Calhoun, V. D. Lateralization of resting state networks and relationship to age and gender. *NeuroImage* **104**, 310–325 (2015).

[6] Ocklenburg, S., Friedrich, P., Güntürkün, O. & Genç, E. Intrahemispheric white matter asymmetries: the missing link between brain structure and functional lateralization? *Rev. Neurosci.* **27**, 465–480 (2016).

[7] Barrick, T. R., Lawes, I. N., Mackay, C. E. & Clark, C. A. White Matter Pathway Asymmetry Underlies Functional Lateralization. *Cereb. Cort.* **17**, 591–598 (2006).

[8] Sun, T. & Walsh, C. A. Molecular approaches to brain asymmetry and handedness. *Nat. Rev. Neur.* **7**, 655–662 (2006).

[9] Roe, J. M. *et al.* Asymmetric thinning of the Cereb. Cort. across the adult lifespan is accelerated in Alzheimer's disease. *Nat. Comm.* **12**, 721 (2021).

[10] Thompson, P. M. *et al.* The enigma consortium: large-scale collaborative analyses of neuroimaging and genetic data. *Brain Img. & Beh.* **8**, 153–182 (2014).

[11] Li, P. *et al.* Hemispheric asymmetry in the human brain and in parkinson's disease is linked to divergent epigenetic patterns in neurons. *Gen. Bio.* **21**, 1–23 (2020).

[12] Kong, X.-Z. *et al.* Mapping cortical and subcortical asymmetry in obsessive-compulsive disorder: findings from the enigma consortium. *Bio. Psych.* **87**, 1022–1034 (2020).

[13] Kong, X.-Z. *et al.* Mapping brain asymmetry in health and disease through the enigma consortium. *HBM* **43**, 167–181 (2022).

[14] Schijven, D. *et al.* Large-scale analysis of structural brain asymmetries in schizophrenia via the enigma consortium. *PNAS* **120**, e2213880120 (2023).

[15] Maximov, I. I. & Westlye, L. T. Comparison of different neurite density metrics with brain asymmetry evaluation. *Zeitschr. Med. Phy.* (2023).

[16] Ardekani, S., Kumar, A., Bartzokis, G. & Sinha, U. Exploratory voxel-based analysis of diffusion indices and hemispheric asymmetry in normal aging. *MRI* **25**, 154–167 (2007).

[17] Franke, K. & Gaser, C. Ten years of brainage as a neuroimaging biomarker of brain aging: what insights have we gained? *Front. Neur.* 789 (2019).

[18] Kaufmann, T. *et al.* Common brain disorders are associated with heritable patterns of apparent aging of the brain. *Nat. Neur.* **22**, 1617–1623 (2019).

[19] Beck, D. *et al.* White matter microstructure across the adult lifespan: A mixed longitudinal and cross-sectional study using advanced diffusion models and brain-age prediction. *NeuroImage* **224**, 117441 (2021).

[20] Beck, D. *et al.* Adipose tissue distribution from body MRI is associated with cross-sectional and longitudinal brain age in adults. *NeuroImage: Clin.* **33**, 102949 (2022).

[21] Korbmacher, M. *et al.* Brain-wide associations between white matter and age highlight the role of fornix microstructure in brain ageing. *HBM* **44** (2023).

[22] Richard, G. *et al.* Brain age prediction in stroke patients: Highly reliable but limited sensitivity to cognitive performance and response to cognitive training. *NeuroImage: Clin.* **25**, 102159 (2020).

[23] de Lange, A.-M. G. *et al.* The maternal brain: Region-specific patterns of brain aging are traceable decades after childbirth. *HBM* **41**, 4718–4729 (2020).

[24] Voldsbekk, I. *et al.* A history of previous childbirths is linked to women's white matter brain age in midlife and older age. *HBM* **42**, 4372–4386 (2021).

[25] Richard, G. *et al.* Assessing distinct patterns of cognitive aging using tissue-specific brain age prediction based on diffusion tensor imaging and brain morphometry. *PeerJ* **6**, e5908 (2018).

[26] Cole, J. H. Multimodality neuroimaging brain-age in uk biobank: relationship to biomedical, lifestyle, and cognitive factors. *Neurobio. Aging* **92**, 34–42 (2020).

[27] De Lange, A.-M. G. *et al.* Multimodal brain-age prediction and cardiovascular risk: The Whitehall II MRI sub-study. *NeuroImage* **222**, 117292 (2020).

[28] Good, C. D. *et al.* Cerebral asymmetry and the effects of sex and handedness on brain structure: a voxel-based morphometric analysis of 465 normal adult human brains. *NeuroImage* **14**, 685–700 (2001).

[29] Jang, H., Lee, J. Y., Lee, K. I. & Park, K. M. Are there differences in brain morphology according to handedness? *Brain & Beh.* **7**, e00730 (2017).

[30] Ocklenburg, S. *et al.* Polygenic scores for handedness and their association with asymmetries in brain structure. *Brain Struct. & Funct.* 1–13 (2021).

[31] Rentería, M. E. Cerebral asymmetry: a quantitative, multifactorial, and plastic brain phenotype. *Twin Res. & Hum. Gen.* **15**, 401–413 (2012).

[32] Benson, R. *et al.* Language dominance determined by whole brain functional mri in patients with brain lesions. *Neurol.* **52**, 798–798 (1999).

[33] Williams, C. M., Peyre, H., Toro, R. & Ramus, F. Comparing brain asymmetries independently of brain size. *NeuroImage* **254**, 119118 (2022).

[34] Jirsaraie, R. J. *et al.* Benchmarking the generalizability of brain age models: challenges posed by scanner variance and prediction bias. *HBM* **44**, 1118–1128 (2023).

[35] Korbmacher, M. *et al.* Considerations on brain age predictions from repeatedly sampled data across time. *Brain & Beh.* **13**, 1–8 (2023).

[36] Nosek, B. A., Ebersole, C. R., DeHaven, A. C. & Mellor, D. T. The preregistration revolution. *PNAS* **115**, 2600–2606 (2018).

[37] Nosek, B. A. *et al.* Preregistration is hard, and worthwhile. *Trends Cog. Sci* **23**, 815–818 (2019).

[38] Beck, D. *et al.* Cardiometabolic risk factors associated with brain age and accelerate brain ageing. *HBM* **43**, 700–720 (2022).

[39] Korbmacher, M. *et al.* Bio-psycho-social factors' associations with brain age: a large-scale uk biobank diffusion study of 35,749 participants. *Front. Psych.* **14**, 1117732 (2023).

[40] Leonardsen, E. H. *et al.* Deep neural networks learn general and clinically relevant representations of the ageing brain. *NeuroImage* **256**, 119210 (2022).

[41] Smith, S. M. *et al.* Brain aging comprises many modes of structural and functional change with distinct genetic and biophysical associations. *eLife* **9**, e52677 (2020).

[42] Sanford, N. *et al.* Sex differences in predictors and regional patterns of brain age gap estimates. *HBM* **43**, 4689–4698 (2022).

[43] Subramaniapillai, S. *et al.* Sex-and age-specific associations between cardiometabolic risk and white matter brain age in the uk biobank cohort. *HBM* **43**, 3759–3774 (2022).

[44] Koen, J. D. & Rugg, M. D. Neural dedifferentiation in the aging brain. *Trends Cog. Sci.* **23**, 547–559 (2019).

[45] Büchel, C. *et al.* White matter asymmetry in the human brain: a diffusion tensor MRI study. *Cereb. Cort.* **14**, 945–951 (2004).

[46] Mito, R. *et al.* Fibre-specific white matter reductions in alzheimer's disease and mild cognitive impairment. *Brain* **141**, 888–902 (2018).

[47] Takao, H., Hayashi, N. & Ohtomo, K. White matter asymmetry in healthy individuals: a diffusion tensor imaging study using tract-based spatial statistics. *Neurosci.* **193**, 291–299 (2011).

[48] Song, J. W. *et al.* Asymmetry of White Matter Pathways in Developing Human Brains. *Cereb. Cortex* **25**, 2883–2893 (2014).

[49] Huang, K. *et al.* Asymmetrical alterations of grey matter among psychiatric disorders: a systematic analysis by voxel-based activation likelihood estimation. *Prog. Neuro-Psychopharm. & Bio. Psych.* **110**, 110322 (2021).

[50] Toga, A. W. & Thompson, P. M. Mapping brain asymmetry. *Nat. Rev. Neuro.* **4**, 37–48 (2003).

[51] Chiarello, C., Vazquez, D., Felton, A. & McDowell, A. Structural asymmetry of the human cereb. cort.: Regional and between-subject variability of surface area, cortical thickness, and local gyrification. *Neuropsychologia* **93**, 365–379 (2016).

[52] Di Biase, M. A. *et al.* Mapping human brain charts cross-sectionally and longitudinally. *PNAS* **120**, e2216798120 (2023).

[53] Button, K. S. *et al.* Power failure: why small sample size undermines the reliability of neuroscience. *Nat. Rev. Neuro.* **14**, 365–376 (2013).

[54] Taki, Y. *et al.* Correlations among brain gray matter volumes, age, gender, and hemisphere in healthy individuals. *PloS one* **6**, e22734 (2011).

[55] Bethlehem, R. A. *et al.* Brain charts for the human lifespan. *Nat.* **604**, 525–533 (2022).

[56] Wei, Y., Zhang, H. & Liu, Y. Charting Normative Brain Variability Across the Human Lifespan. *Neurosci. Bull.* **39**, 362–364 (2023).

[57] Westlye, L. T. *et al.* Life-span changes of the human brain white matter: diffusion tensor imaging (DTI) and volumetry. *Cereb. Cort.* **20**, 2055–2068 (2010).

[58] Korbmacher, M. *et al.* Distinct longitudinal brain white matter microstructure changes and associated polygenic risk of common psychiatric disorders and alzheimer's disease in the uk biobank. *medRxiv (Preprint)* (2023).

[59] Xiao, D., Wang, K., Theriault, L., Charbel, E. & Initiative, A. D. N. White matter integrity and key structures affected in alzheimer's disease characterized by diffusion tensor imaging. *Eur. J. Neurosci.* **56**, 5319–5331 (2022).

[60] Rajmohan, V. & Mohandas, E. The limbic system. *Ind J Psych* **49**, 132 (2007).

[61] Redlich, R. *et al.* The limbic system in youth depression: brain structural and functional alterations in adolescent in-patients with severe depression. *Neuropsychopharm.* **43**, 546–554 (2018).

[62] Zelikowsky, M., Hersman, S., Chawla, M. K., Barnes, C. A. & Fanselow, M. S. Neuronal ensembles in amygdala, hippocampus, and prefrontal cortex track differential components of contextual fear. *J Neurosc* **34**, 8462–8466 (2014).

[63] Bari, A., Niu, T., Langevin, J.-P. & Fried, I. Limbic neuromodulation: implications for addiction, posttraumatic stress disorder, and memory. *Neurosurg. Clin.* **25**, 137–145 (2014).

[64] Coupé, P., Manjón, J. V., Lanuza, E. & Catheline, G. Lifespan changes of the human brain in alzheimer's disease. *Sci. Rep.* **9**, 3998 (2019).

[65] Yamada, S., Ishikawa, M. & Nozaki, K. Exploring mechanisms of ventricular enlargement in idiopathic normal pressure hydrocephalus: a role of cerebrospinal fluid dynamics and motile cilia. *Flu. Barr. CNS* **18**, 1–11 (2021).

[66] Schoenfeld, T. J. & Cameron, H. A. Adult neurogenesis and mental illness. *Neuropsychophar.* **40**, 113–128 (2015).

[67] Peyton, L., Oliveros, A., Choi, D.-S. & Jang, M.-H. Hippocampal regenerative medicine: neurogenic implications for addiction and mental disorders. *Exp. & Mol. Med.* **53**, 358–368 (2021).

[68] Moodley, K. & Chan, D. The hippocampus in neurodegenerative disease. *Hippo. Clin. Neurosci.* **34**, 95–108 (2014).

[69] Van de Pol, L. *et al.* Hippocampal atrophy in alzheimer disease: age matters. *Neurol.* **66**, 236–238 (2006).

[70] Van Hecke, W., Emsell, L., Sunaert, S. *et al. Diffusion tensor imaging: a practical handbook* (Springer, 2016).

[71] Huster, R. J., Westerhausen, R., Kreuder, F., Schweiger, E. & Wittling, W. Morphologic asymmetry of the human anterior cingulate cortex. *NeuroImage* **34**, 888–895 (2007).

[72] Kucyi, A., Moayedi, M., Weissman-Fogel, I., Hodaie, M. & Davis, K. D. Hemispheric asymmetry in white matter connectivity of the temporoparietal junction with the insula and prefrontal cortex. *PloS one* **7**, e35589 (2012).

[73] Wang, J. *et al.* Asymmetry of the dorsal anterior cingulate cortex: evidences from multiple modalities of mri. *Neuroinf.* **11**, 149–157 (2013).

[74] Takahashi, T. *et al.* Lack of normal structural asymmetry of the anterior cingulate gyrus in female patients with schizophrenia: a volumetric magnetic resonance imaging study. *Schiz. Res.* **55**, 69–81 (2002).

[75] Manoach, D. S. *et al.* Reduced microstructural integrity of the white matter underlying anterior cingulate cortex is associated with increased saccadic latency in schizophrenia. *NeuroImage* **37**, 599–610 (2007).

[76] Joo, S. W. *et al.* Abnormal asymmetry of white matter tracts between ventral posterior cingulate cortex and middle temporal gyrus in recent-onset schizophrenia. *Schiz. Res.* **192**, 159–166 (2018).

[77] Zhao, X. *et al.* Reduced interhemispheric white matter asymmetries in medial temporal lobe epilepsy with hippocampal sclerosis. *Front. Neurol.* **10**, 394 (2019).

[78] Zhang, Y. *et al.* Study of the microstructure of brain white matter in medial temporal lobe epilepsy based on diffusion tensor imaging. *Brain & Beh.* **13**, e2919 (2023).

[79] Cattarinussi, G. *et al.* White matter microstructure associated with the antidepressant effects of deep brain stimulation in treatment-resistant depression: A review of diffusion tensor imaging studies. *Int. J. Molec. Sci.* **23**, 15379 (2022).

[80] Xu, J. *et al.* Effects of urban living environments on mental health in adults. *Nat. Med.* 1–12 (2023).

[81] Chan, M. Y. *et al.* Long-term prognosis and educational determinants of brain network decline in older adult individuals. *Nat. aging* **1**, 1053–1067 (2021).

[82] Schoeler, T. *et al.* Participation bias in the uk biobank distorts genetic associations and downstream analyses. *Nat. Hum. Beh.* 1–12 (2023).

[83] Lyall, D. M. *et al.* Quantifying bias in psychological and physical health in the uk biobank imaging sub-sample. *Brain Comm.* **4**, fcac119 (2022).

[84] Alfaro-Almagro, F. *et al.* Image processing and quality control for the first 10,000 brain imaging datasets from uk biobank. *NeuroImage* **166**, 400–424 (2018).

[85] Maximov, I. I. *et al.* Fast qualitY conTrol meThod foR derIved diffUsion Metrics (YTTRIUM) in big data analysis: UK Biobank 18,608 example. *HBM* **42**,

3141–3155 (2021).

[86] Rosen, A. F. *et al.* Quantitative assessment of structural image quality. *NeuroImage* **169**, 407–418 (2018).

[87] Wang, Z., Bovik, A. C., Sheikh, H. R. & Simoncelli, E. P. Image quality assessment: from error visibility to structural similarity. *IEEE Transact. Img. Proc.* **13**, 600–612 (2004).

[88] Brunet, D., Vrscay, E. R. & Wang, Z. On the mathematical properties of the structural similarity index. *IEEE Transact. Img. Proc.* **21**, 1488–1499 (2011).

[89] Miller, K. L. *et al.* Multimodal population brain imaging in the UK Biobank prospective epidemiological study. *Nat. Neur.* **19**, 1523–1536 (2016).

[90] Sudlow, C. *et al.* UK biobank: an open access resource for identifying the causes of a wide range of complex diseases of middle and old age. *PLoS Med.* **12**, e1001779 (2015).

[91] Veraart, J., Fieremans, E. & Novikov, D. S. Diffusion MRI noise mapping using random matrix theory. *MR in Med.* **76**, 1582–1593 (2016).

[92] Kellner, E., Dhital, B., Kiselev, V. G. & Reisert, M. Gibbs-ringing artifact removal based on local subvoxel-shifts. *MR in Med.* **76**, 1574–1581 (2016).

[93] Andersson, J. L. & Sotiropoulos, S. N. An integrated approach to correction for off-resonance effects and subject movement in diffusion MR imaging. *NeuroImage* **125**, 1063–1078 (2016).

[94] Smith, S. M. *et al.* Advances in functional and structural MR image analysis and implementation as FSL. *NeuroImage* **23**, S208–S219 (2004).

[95] Jenkinson, M., Beckmann, C. F., Behrens, T. E., Woolrich, M. W. & Smith, S. M. FSL. *NeuroImage* **62**, 782–790 (2012).

[96] Basser, P. J., Mattiello, J. & LeBihan, D. Mr diffusion tensor spectroscopy and imaging. *Biophys. J.* **66**, 259–267 (1994).

[97] Jensen, J. H., Helpern, J. A., Ramani, A., Lu, H. & Kaczynski, K. Diffusional kurtosis imaging: the quantification of non-gaussian water diffusion by means of magnetic resonance imaging. *MR in Med.* **53**, 1432–1440 (2005).

[98] Fieremans, E., Jensen, J. H. & Helpern, J. A. White matter characterization with diffusional kurtosis imaging. *NeuroImage* **58**, 177–188 (2011).

[99] Kaden, E., Kruggel, F. & Alexander, D. C. Quantitative mapping of the per-axon diffusion coefficients in brain white matter. *MR in Med.* **75**, 1752–1763 (2016).

[100] Kaden, E., Kelm, N. D., Carson, R. P., Does, M. D. & Alexander, D. C. Multi-compartment microscopic diffusion imaging. *NeuroImage* **139**, 346–359 (2016).

[101] Reisert, M., Kellner, E., Dhital, B., Hennig, J. & Kiselev, V. G. Disentangling micro from mesostructure by diffusion MRI: a Bayesian approach. *NeuroImage* **147**, 964–975 (2017).

[102] Fischl, B. Freesurfer. *NeuroImage* **62**, 774–781 (2012).

[103] Dale, A. M., Fischl, B. & Sereno, M. I. Cortical surface-based analysis: I. Segmentation and surface reconstruction. *NeuroImage* **9**, 179–194 (1999).

[104] Smith, S. M. *et al.* Tract-based spatial statistics: voxelwise analysis of multi-subject diffusion data. *NeuroImage* **31**, 1487–1505 (2006).

[105] Smith, S. M. Fast robust automated brain extraction. *HBM* **17**, 143–155 (2002).

[106] Mori, S., Wakana, S., Nagae-Poetscher, L. & Van Zijl, P. MRI atlas of human white matter. *Am. J. Neurorad.* **27**, 1384 (2006).

[107] Hua, K. *et al.* Tract probability maps in stereotaxic spaces: analyses of white matter anatomy and tract-specific quantification. *NeuroImage* **39**, 336–347 (2008).

[108] Desikan, R. S. *et al.* An automated labeling system for subdividing the human Cereb. Cort. on MRI scans into gyral based regions of interest. *NeuroImage* **31**, 968–980 (2006).

[109] Chen, T. & Guestrin, C. *Xgboost: A scalable tree boosting system*, 785–794 (2016).

[110] de Lange, A.-M. G. & Cole, J. H. Commentary: Correction procedures in brain-age prediction. *NeuroImage: Clin.* **26** (2020).

[111] de Lange, A.-M. G. *et al.* Mind the gap: Performance metric evaluation in brain-age prediction. *HBM* **43**, 3113–3129 (2022).

[112] Lehmann, E. L. On likelihood ratio tests. *Selected works of E.L. Lehmann* 209–216 (2012).

[113] Akaike, H. in *Information theory and an extension of the maximum likelihood principle* 199–213 (Springer, 1998).

[114] Neath, A. A. & Cavanaugh, J. E. The bayesian information criterion: background, derivation, and applications. *Wiley Interdisc. Rev.: Comp. Stat.* **4**, 199–203 (2012).

[115] Maechler, M., Maechler, M. M., MPFR, S., Suggests, M. & SuggestsNote, M. Package 'rmpfr'. *CRAN* (2016). URL https://cran.r-project.org/web/packages/Rmpfr/index.html.

ACKNOWLEDGEMENTS

This study has been conducted using UKB data under Application 27412. UKB has received ethics approval from the National Health Service National Research Ethics Service (ref 11/NW/0382). The work was performed on the Service for Sensitive Data (TSD) platform, owned by the University of Oslo, operated and developed by the TSD service group at the University of Oslo IT-Department (USIT). Computations were performed using resources provided by UNINETT Sigma2 – the National Infrastructure for High Performance Computing and Data Storage in Norway.

We want to thank Tobias Kaufmann and Torgeir Moberget who processed the T_1-weighted MRI data, and all UKB participants and facilitators who made this research possible.

This research was funded by the Research Council of Norway (#223273); the South-Eastern Norway Regional Health Authority (#2022080); and the European Union's Horizon2020 Research and Innovation Programme (CoMorMent project; Grant #847776).

AUTHOR CONTRIBUTIONS

M.K..: Study design, Software, Formal analysis, Visualizations, Project administration, Writing—original draft, Writing—review & editing. D.v.d.M.: Software, Writing – review & editing. D.B.: Writing—review & editing. A.M.d.L.: Software, Writing—review & editing. A.L.: Funding acquisition. E.E.: Funding acquisition. O.A.A.: Writing—review & editing, Funding acquisition. L.T.W.: Writing—review & editing, Funding acquisition. I.I.M.: Supervision, Study design, Data preprocessing and quality control, Writing—review & editing, Funding acquisition.

COMPETING INTERESTS

OAA has received a speaker's honorarium from Lundbeck and is a consultant to Coretechs.ai. We declare no other conflicts of interest.

887 # FIGURES

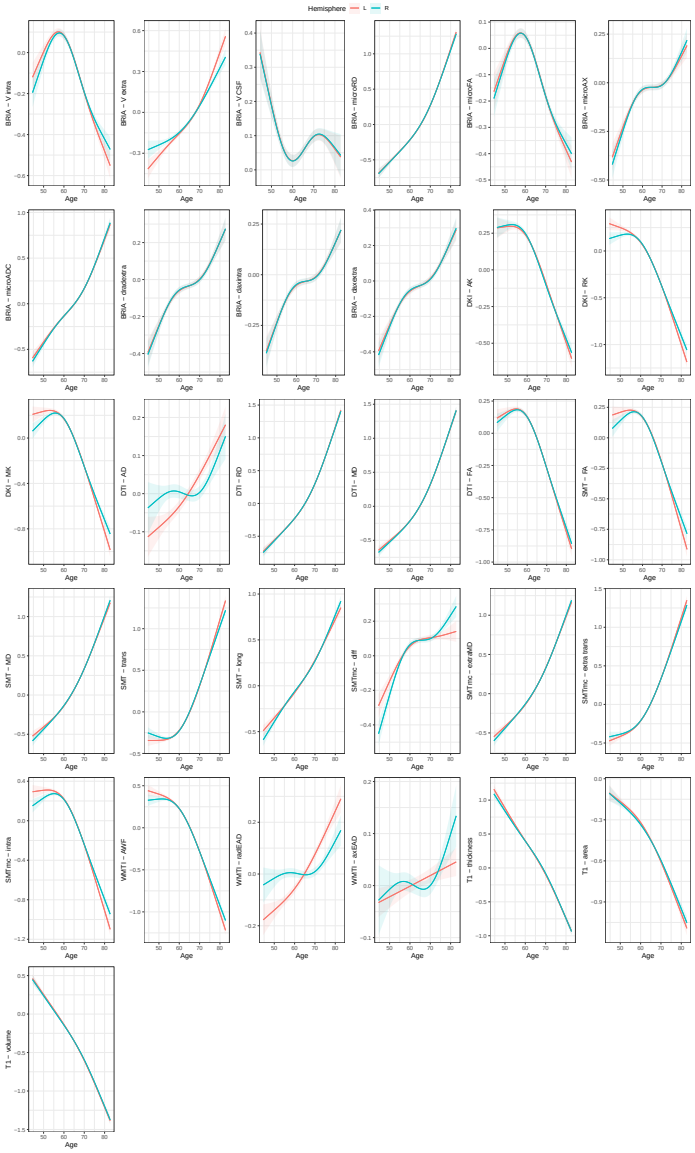

Fig. 1 Age curves of standardized and zero-centered mean values of GM and WM features per hemisphere. A cubic smooth function (s) with $k = 4$ knots was applied to plot the relationship between age and brain features correcting for sex and scanner site (F): $\hat{age} = s(F) + sex + site$ using restricted maximum likelihood (REML). The grey shaded area indicates the 95% CI. All age-relationships were significant ($p_{adj} < .05$).

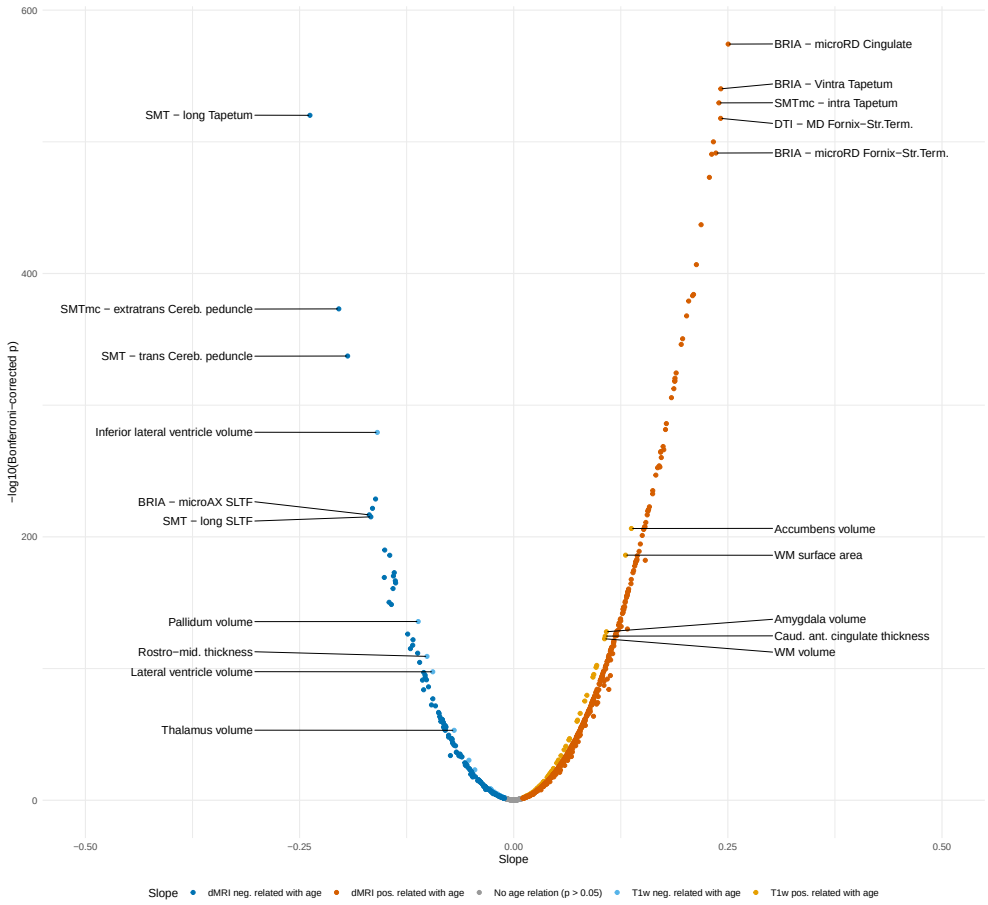

Fig. 2 T_1-weighted and dMRI features linear asymmetry-age-associations. The plot presents the standardized (sex- and site-corrected) regression slopes versus Bonferroni-adjusted -log10 p-values. Modelling was done using Eq. 2: $\hat{age} = \beta_0 + \beta_1 \times F + \beta_2 \times Sex + \beta_3 \times Site$, where F is the respective brain feature. Labelling was done separately for T_1-weighted and dMRI indicating the 10 most significantly associated features (five for $\beta > 0$ and five for $\beta < 0$). ILF = inferior longitudinal fasciculus, Cereb.Peduncle = cerebral peduncle, Rostro-mid. thicknes = rostro-middle thickness, SLFT = superior longitudinal fasciculus (temporal part), Fornix-Str.Term. = fornix-stria terminalis tract, Caud. ant. cingulate = caudal anterior cingulate. Full tables are available at https://github.com/MaxKorbmacher/Hemispheric_Brain_Age/.

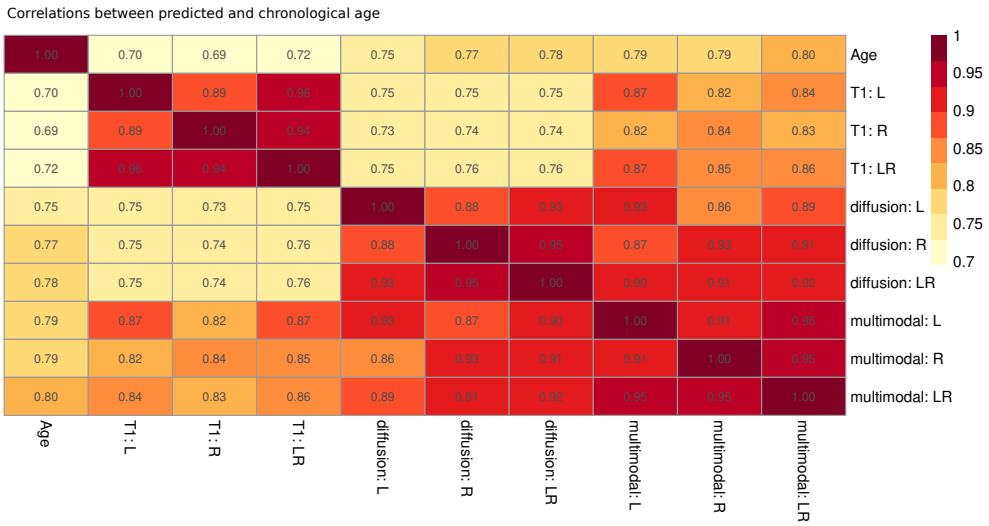

Fig. 3 Pearson correlation coefficients between chronological and predicted ages for T_1-weighted, diffusion, and multimodal MRI for left, right and both hemispheres. All Bonferroni-corrected $p < .001$. L: left hemisphere, R: right hemisphere, LR: both hemispheres.

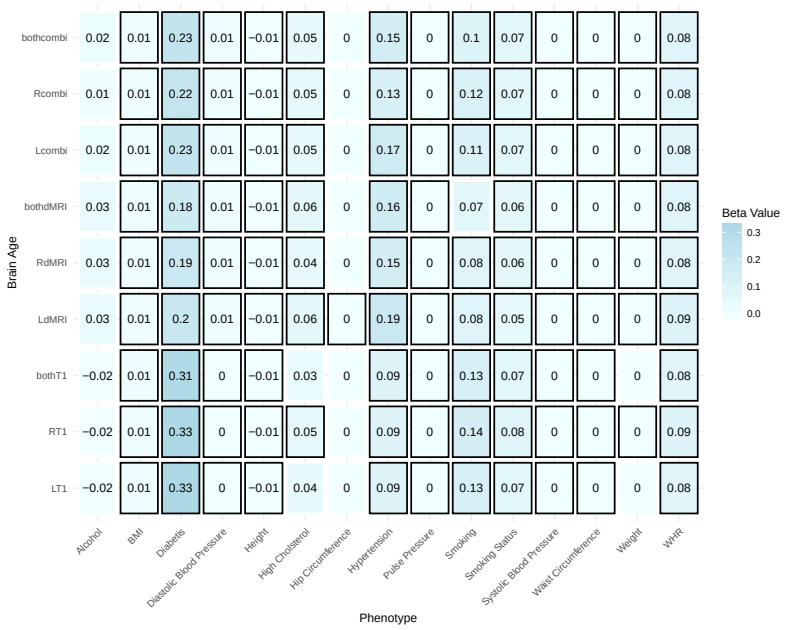

Fig. 4 Linear association between general health-and-lifestyle phenotypes and brain age estimated from different modalities, left, right and both hemispheres. Eq. 9 was used and standardized slopes are presented. For simplicity, standardized slopes with $|\beta| < 0.005$ were rounded down to $\beta = 0$. L: left hemisphere, R: right hemisphere, LR: both hemispheres, BMI: body mass index, WHR: waist-to-hip ratio. Bonferroni-adjusted $p < .05$ is marked by a black frame.

TABLES

Table 1 Hemispheric brain age prediction outcomes.

Model	Features	R^2	MAE	RMSE	Correlation*
Left T_1w	117	0.504 (0.010)	4.389 (0.054)	5.472 (0.061)	0.708 [0.703, 0.712]
Right T_1w	117	0.492 (0.008)	4.439 (0.049)	5.529 (0.051)	0.705 [0.700, 0.709]
T_1w	234	0.526 (0.011)	4.294 (0.050)	5.356 (0.062)	0.725 [0.721, 0.730]
Left dMRI	840	0.568 (0.014)	4.000 (0.047)	4.990 (0.067)	0.757 [0.753, 0.762]
Right dMRI	840	0.582 (0.013)	3.960 (0.052)	4.967 (0.079)	0.766 [0.762, 0.771]
dMRI	1680	0.605 (0.010)	3.867 (0.059)	4.821 (0.094)	0.781 [0.777, 0.785]
Left multimodal	957	0.630 (0.009)	3.757 (0.046)	4.673 (0.047)	0.794 [0.790, 0.797]
Right multimodal	957	0.634 (0.014)	3.723 (0.073)	4.673 (0.092)	0.794 [0.791, 0.798]
Multimodal	1914	0.628 (0.017)	3.663 (0.055)	4.563 (0.077)	0.793 [0.789, 0.797]

R^2 = Variance explained, MAE = Mean Absolute Error, RMSE = Root Mean Squared Error, Corr. = Correlation, Values in round parentheses () refer to standard deviations and square brackets [] to 95% confidence interval around correlations (Pearson's r) of uncorrected brain age estimates and chronological age.

* The correlation between raw brain age and chronological age.

SUPPLEMENTARY INFORMATION

Supplementary information to the article "Brain asymmetries from mid- to late-life and hemispheric brain age", Korbmacher et al., 2023

SUPPLEMENTARY TABLES

1 Tuned hyperparameters for brain age models considering both sexes together

Overview of the tuned hyperparameters for each of the used brain age models considering both sexes together.

Modality	Hemisphere	Learning Rate	Maximum Depth	Number of Trees
Multimodal	Both	0.1	8	140
Multimodal	Left	0.05	7	180
Multimodal	Right	0.1	8	140
dMRI	Both	0.1	6	100
dMRI	Left	0.1	4	180
dMRI	Right	0.1	5	180
T_1w	Both	0.1	5	140
T_1w	Left	0.1	6	140
T_1w	Right	0.1	6	180

2 Most age-sensitive regional features using non-linear models

T_1 Metric	Deviance	F	dMRI Metric	Deviance	F
superior temporal thickness (lh)	587304.16	4188.91	DKI - AK anterior limb of the internal capsule (rh)	644106.76	5170.95
hippocampus volume (rh)	576250.86	4101.39	DTI - RD fornix striaterminalis (rh)	627313.71	4981.99
thickness (lh)	576355.10	4082.87	DTI - FA anterior corona radiata (lh)	571637.61	4390.91
inferiorparietal thickness (lh)	569468.00	4041.74	DTI - FA inferior fronto-occipital fasciculus (lh)	568799.27	4366.64
hippocampus volume (lh)	565456.80	4006.59	BRIA - microRD anterior thalamic radiation (rh)	561902.12	4295.66
thickness (rh)	562548.97	3965.59	WMTI - radEAD anterior coronaradiata (rh)	433925.45	4281.90
inferior lateral ventricle volume (lh)	544864.71	3836.12	BRIA - microFA fornix striaterminalis (rh)	557084.22	4247.55
inferior lateral ventricle volume (rh)	539066.94	3786.01	DTI - FA fornix striaterminalis (rh)	545272.55	4125.27
superior temporal thickness (rh)	522564.64	3603.62	BRIA - microRD fornix striaterminalis (rh)	539180.21	4070.72
lateral ventricle volume (lh)	513713.08	3567.34	BRIA - microADC anterior thalamic radiation (rh)	536979.62	4050.30

3 Most age-sensitive regional features using linear models

T_1 Metric	Sum of Squares	F	dMRI Metric	Sum of Squares	F
superior temporal thickness (lh)	582215.80	12516.42	DTI - RD fornix striaterminalis (rh)	568838.72	13114.24
thickness (lh)	571936.88	12239.14	DTI - FA anterior coronaradiata (lh)	554045.66	12664.20
hippocampus volume (rh)	564806.62	12048.28	DTI - FA inferior fronto-occipital fasciculus (lh)	527205.85	11866.98
inferiorparietal thickness (rh)	559834.17	11915.90	DTI - FA fornix striaterminalis (rh)	526713.03	11852.57
thickness (rh)	557696.94	11859.18	DTI - RD anterior coronaradiata (lh)	504149.35	11201.30
hippocampus volume (lh)	554478.02	11773.95	DTI - RD anterior coronaradiata (rh)	500047.51	11084.67
superior temporal thickness (rh)	519361.12	10859.68	DTI - FA anterior coronaradiata (rh)	481860.37	10573.93
thalamus volume (rh)	470220.77	9626.25	BRIA - microRD anterior thalamic radiation (rh)	480010.76	10522.57
cortex volume (lh)	455643.18	9270.23	DTI - RD inferior fronto-occipital fasciculus (lh)	471710.65	10293.35
amygdala (lh)	454268.29	9236.88	DTI - FA inferior fronto-occipital fasciculus (rh)	470227.52	10252.62

4 Global metrics' age sensitivity using linear models

LRTs outcomes testing global metrics' age sensitivity using linear models (Eqs. 2 & 4), with p-values being Bonferroni-corrected for multiple comparison. Acronyms lh and rh refer to mean left and right hemisphere, respectively.

Metric	Sum of Squares	F	p	Metric	Sum of Squares	F	p
BRIA vintra (lh)	-14143.51	256.78	<.001	*DTI MD (rh)*	-294821.39	6256.88	<.001
BRIA vintra (rh)	-13492.91	244.88	<.001	*DTI FA (lh)*	-294054.08	6237.71	<.001
BRIA vextra (lh)	-8868.68	160.58	<.001	*DTI FA (rh)*	-290846.08	6157.77	<.001
BRIA vextra (rh)	-8247.91	149.29	<.001	*SMT FA (lh)*	-96237.02	1824.32	<.001
BRIA vcsf (lh)	-12339.56	223.82	<.001	*SMT FA (rh)*	-88924.97	1679.10	<.001
BRIA vcsf (rh)	-11691.20	211.99	<.001	*SMT MD (lh)*	-145717.99	2837.80	<.001
BRIA micrord (lh)	-110749.44	2115.93	<.001	*SMT MD (rh)*	-138236.90	2681.03	<.001
BRIA micrord (rh)	-112757.19	2156.64	<.001	*SMT trans (lh)*	-236947.06	4859.34	<.001
BRIA microfa (lh)	-7389.49	133.69	<.001	*SMT trans (rh)*	-230976.33	4720.50	<.001
BRIA microfa (rh)	-7660.08	138.61	<.001	*SMT long (lh)*	-233251.22	4773.28	<.001
BRIA microax (lh)	-20330.95	370.29	<.001	*SMT long (rh)*	-221802.60	4509.03	<.001
BRIA microax (rh)	-19217.81	349.82	<.001	*SMTmc d (lh)*	-12811.82	232.44	<.001
BRIA microadc (lh)	-244852.70	5044.67	<.001	*SMTmc d (rh)*	-15325.44	278.40	<.001
BRIA microadc (rh)	-242965.40	5000.27	<.001	*SMTmc extramd (lh)*	-234164.26	4794.51	<.001
BRIA dradextra (lh)	-0.87	0.02	1.00	*SMTmc extramd (rh)*	-221755.78	4507.96	<.001
BRIA dradextra (rh)	-0.56	0.01	1.00	*SMTmc extratrans (lh)*	-269921.51	5643.84	<.001
BRIA daxintra (lh)	-45776.98	844.85	<.001	*SMTmc extratrans (rh)*	-251971.27	5213.02	<.001
BRIA daxintra (rh)	-32572.59	597.02	<.001	*SMTmc intra (lh)*	-162286.59	3189.66	<.001
BRIA daxextra (lh)	-33941.70	622.56	<.001	*SMTmc intra (rh)*	-138122.05	2678.64	<.001
BRIA daxextra (rh)	-29058.51	531.64	<.001	*WMTI awf (lh)*	-216212.24	4381.26	<.001
DKI AK (lh)	-98394.96	1867.39	<.001	*WMTI awf (rh)*	-198966.98	3992.24	<.001
DKI AK (rh)	-107687.41	2054.02	<.001	*WMTI radead (lh)*	-538.93	9.72	0.11
DKI RK (lh)	-134762.36	2608.66	<.001	*WMTI radead (rh)*	-1786.25	32.22	<.001
DKI RK (rh)	-117109.00	2245.17	<.001	*WMTI axead (lh)*	-15537.30	282.28	<.001
DKI MK (lh)	-166559.26	3281.46	<.001	*WMTI axead (rh)*	-140593.59	2730.28	<.001
DKI MK (rh)	-146629.45	2856.99	<.001	*T1 (lh) thickness*	-361976.02	7460.14	<.001
DTI AD (lh)	-6414.25	115.99	<.001	*T1 (rh) thickness*	-337720.79	6873.27	<.001
DTI AD (rh)	-32682.00	599.06	<.001	*T1 (lh) area*	-131984.99	2428.71	<.001
DTI RD (lh)	-103169.79	1963.06	<.001	*T1 (rh) area*	-115500.16	2109.17	<.001
DTI RD (rh)	-98654.94	1872.59	<.001	*T1 (lh) volume*	-366138.06	7562.34	<.001
DTI MD (lh)	-296264.43	6292.97	<.001	*T1 (rh) volume*	-351072.41	7194.50	<.001

5 Global metrics' age sensitivity using non-linear models

LRTs outcomes testing global metrics' age sensitivity using generalized additive models (Eqs. (3,4)), with p-values being Bonferroni-corrected for multiple comparison. Acronyms lh and rh refer to mean left and right hemisphere, respectively.

Metric	Deviance	F	p	Metric	Deviance	F	p
BRIA vintra (lh)	298222.11	1980.42	<.001	*DTI MD (rh)*	420292.82	2975.29	<.001
BRIA vintra (rh)	263814.46	1721.75	<.001	*DTI FA (lh)*	454980.03	3284.21	<.001
BRIA vextra (lh)	99954.26	601.06	<.001	*DTI FA (rh)*	437831.65	3130.91	<.001
BRIA vextra (rh)	68415.48	404.41	<.001	*SMT FA (lh)*	231126.97	1481.17	<.001
BRIA vcsf (lh)	389707.46	2715.85	<.001	*SMT FA (rh)*	212502.18	1350	<.001
BRIA vcsf (rh)	395906.41	2768.18	<.001	*SMT MD (lh)*	338666.06	2295.03	<.001
BRIA micrord (lh)	489922	3605.08	<.001	*SMT MD (rh)*	329913.59	2225.14	<.001
BRIA micrord (rh)	482669.31	3537.29	<.001	*SMT trans (lh)*	325557.05	2188.8	<.001
BRIA microfa (lh)	468131.01	3399.04	<.001	*SMT trans (rh)*	309770.56	2066.61	<.001
BRIA microfa (rh)	441798.75	3161.43	<.001	*SMT long (lh)*	239399.25	1543.22	<.001
BRIA microax (lh)	123284.12	747.18	<.001	*SMT long (rh)*	220310.81	1406.65	<.001
BRIA microax (rh)	122353.86	741.87	<.001	*SMTmc d (lh)*	17581.83	100.96	<.001
BRIA microadc (lh)	442217.61	3169.41	<.001	*SMTmc d (rh)*	18705.17	107	<.001
BRIA microadc (rh)	433573.24	3092.76	<.001	*SMTmc extramd (lh)*	375805.34	2598.83	<.001
BRIA dradextra (lh)	265199.9	1732.72	<.001	*SMTmc extramd (rh)*	350591.17	2392.53	<.001
BRIA dradextra (rh)	259410.42	1690.27	1.00	*SMTmc extratrans (lh)*	381698.57	2646.36	<.001
BRIA daxintra (lh)	227477.58	1459.06	<.001	*SMTmc extratrans (rh)*	357451.71	2446.62	<.001
BRIA daxintra (rh)	221619.72	1417.52	<.001	*SMTmc intra (lh)*	230534.22	1477.89	<.001
BRIA daxextra (lh)	269452.37	1764.08	<.001	*SMTmc intra (rh)*	196608	1238.41	<.001
BRIA daxextra (rh)	265820.53	1737.25	<.001	*WMTI awf (lh)*	294396.47	1946.39	<.001
DKI AK (lh)	248201.74	1607.19	<.001	*WMTI awf (rh)*	271308.81	1773.47	<.001
DKI AK (rh)	277452.37	1822.07	<.001	*WMTI radead (lh)*	356837.69	2444	<.001
DKI RK (lh)	248246.37	1606.74	<.001	*WMTI radead (rh)*	347896.75	2371.95	<.001
DKI RK (rh)	214591.89	1365.38	<.001	*WMTI axead (lh)*	22893.57	133.33	<.001
DKI MK (lh)	225899.98	1446.06	<.001	*WMTI axead (rh)*	30036.73	175.61	<.001
DKI MK (rh)	190685.71	1195.84	<.001	*T1 (lh) thickness*	363679.29	2447.65	<.001
DTI AD (lh)	91486.87	545.48	<.001	*T1 (rh) thickness*	339637.31	2256.41	<.001
DTI AD (rh)	63150.51	374.43	<.001	*T1 (lh) area*	132330.67	818.92	<.001
DTI RD (lh)	492407	3628.18	<.001	*T1 (rh) area*	115697.02	777.46	<.001
DTI RD (rh)	481438.43	3525.6	<.001	*T1 (lh) volume*	366575.45	2414.26	<.001
DTI MD (lh)	425442.7	3020.18	<.001	*T1 (rh) volume*	351519.39	2312.27	<.001

6 Differences of T_1-weighted and dMRI features between hemispheres by sex

The table shows the ten largest regional differences between left and right hemispheres' T_1-weighted and dMRI data indicated by effect size (Cohen's d) indicated by paired samples t-tests (two-sided) and presented separately for males and females. All Bonferroni corrected $p < .05$. SLFT = Superior longitudinal fasciculus (temporal part), ILF = Inferior longitudinal fasciculus. For full tables see the files Hemi_NEW_sex_dMRI_features_diff.csv and Hemi_NEW_sex_T1w_features_diff.csv at https://github.com/MaxKorbmacher/Hemispheric_Brain_Age.

diffusion MRI

Feature	**Cohen's d_{males}**	**Feature**	**Cohen's $d_{females}$**
DTI - FA ILF	3.44	DTI - FA ILF	3.91
DTI - AD SLFT	2.09	DTI - AD SLFT	2.40
WMTI - axEAD SLFT	2.01	SMTmc - diff SLFT	2.06
DTI - FA cingulate gyrus	1.93	SMT - long SLFT	2.04
DKI - RK cingulate gyrus	1.90	DTI - FA cingulate gyrus	1.98
WMTI - AWF cingulate gyrus	1.83	SMTmc - extratrans cerebral peduncle	1.96
DTI - AD ILF	1.81	SMTmc - extraMD SLFT	1.93
DTI - FA superior frontooccipital fasciculus	1.77	BRIA - microAX SLFT	1.92
DKI - RK SLFT	1.75	DKI - RK SLFT	1.91
SMTmc - extratrans cerebral peduncle	1.74	SMTmc - intra cingulate gyrus	1.89
T_1-weighted MRI			
Feature	**Cohen's d_{males}**	**Feature**	**Cohen's $d_{females}$**
frontal pole area	1.82	transverse temporal area	1.89
pars orbitalis area	1.78	frontal pole area	1.73
transverse temporal area	1.77	pars orbitalis area	1.72
inferior parietal area	1.71	inferior parietal area	1.72
inferior parietal volume	1.62	inferior parietal volume	1.64
frontal pole volume	1.58	frontal pole volume	1.54
thalamus volume	1.40	middle temporal area	1.42
middle temporal area	1.31	transverse temporal volume	1.38
transverse temporal volume	1.29	thalamus volume	1.34
pars orbitalis volume	1.27	pars orbitalis volume	1.29

7 Most age-sensitive regional T_1- and diffusion-weighted features using *non*-linear models *by sex*

The table shows the ten largest regional differences between left and right hemispheres' T_1-weighted and dMRI data indicated by F from LRTs comparing a baseline model (Eq. 4) to the GAM (Eq. 3) presented separately for males and females. All Bonferroni corrected $p < .05$. ATR = Anterior thalamic radiation, IFOF = inferior fronto-occipital fasciculus. For full tables see the files Hemi_NEW_REGIONAL_dMRI_non_linear_hemi_effects_MALES.csv, Hemi_NEW_REGIONAL_dMRI_non_linear_hemi_effects_FEMALES.csv, Hemi_NEW_REGIONAL_T1_non_linear_hemi_effects_MALES.csv, and Hemi_NEW_REGIONAL_T1_non_linear_hemi_effects_FEMALES.csv at https://github.com/MaxKorbmacher/Hemispheric_Brain_Age.

Males

T_1 Metric	Deviance	F	dMRI Metric	Deviance	F
Hippocampus volume (rh)	325396.71	2327.14	DTI - RD fornix striaterminalis (rh)	321483.12	2474.87
Inferior lateral ventricle volume (lh)	315630.20	2242.52	DKI - AK Anteriorlimbofinternalcapsule (rh)	315123.70	2406.94
Hippocampus volume (lh)	314178.29	2222.80	DTI - FA fornix striaterminalis (rh)	287920.97	2127.34
Lateral ventricle volume (rh)	294791.55	2055.25	DTI - FA IFOF (lh)	286229.79	2114.11
Superior temporal thickness (lh)	288883.19	1973.34	BRIA - micro Rd ATR (rh)	285675.67	2109.47
Thickness (lh)	286653.65	1944.76	DTI - FA Anteriorcoronaradiata (lh)	285098.32	2099.07
Thickness (rh)	285659.63	1943.02	BRIA - micro FA Fornix Striaterminalis (rh)	280978.76	2062.43
Lateral ventricle volume (lh)	280759.99	1932.22	BRIA - micro Rd ATR (lh)	268901.80	1946.45
Bankssts thickness (lh)	111534.08	1927.07	DTI - RD ATR (rh)	268857.43	1944.99
Rostral middle frontal volume (rh)	112544.65	1887.40	DTI - RD ATR (lh)	268408.62	1942.57

Females

T_1 Metric	Deviance	F	dMRI Metric	Deviance	F
Superior temporal thickness (lh)	298436.46	2186.28	DKI - AK Anteriorlimbofinternalcapsule (rh)	328299.92	2756.78
Inferior parietal thickness (rh)	294083.30	2157.56	DTI - RD Fornix Striaterminalis (rh)	309568.49	2539.12
Thickness (lh)	289859.17	2098.94	DTI - FA Anteriorcoronaradiata (lh)	287115.30	2288.94
Thickness (rh)	277328.73	1988.89	DTI - FA IFOF (lh)	282230.37	2243.21
Superiortemporal thickness (rh)	268345.92	1902.38	BRIA - micro FA Fornix Striaterminalis (rh)	279454.04	2213.63
Hippocampus volume (lh)	256888.62	1827.15	BRIA - micro Rd Fornix Striaterminalis (rh)	279158.45	2213.20
Hippocampus volume (rh)	256386.19	1820.25	BRIA - micro Rd ATR (rh)	279221.52	2209.87
Lateral ventricle volume (rh)	247973.59	1755.77	DTI - RD ATR (lh)	278213.99	2202.86
Lateral ventricle volume (lh)	237509.49	1666.32	DTI - RD Anteriorcoronaradiata (lh)	277873.07	2197.90
Supramarginal thickness (rh)	235411.09	1632.94	BRIA - micro Rd ATR (lh)	274318.30	2160.44

8 Most age-sensitive regional T_1- and diffusion-weighted features using linear models *by sex*

The table shows the ten largest regional differences between left and right hemispheres' T_1-weighted and dMRI data indicated by F from LRTs comparing a baseline model (Eq. 4) to the linear model (Eq. 2) presented separately for males and females. All Bonferroni corrected $p < .05$. ATR = Anterior thalamic radiation, SLFT = superior longitudinal fasciculus (temporal part), IFOF = inferior fronto-occipital fasciculus. For full tables see the files Hemi_NEW_REGIONAL_dMRI_linear_hemi_effects_MALES.csv, Hemi_NEW_REGIONAL_dMRI_linear_hemi_effects_FEMALES.csv, Hemi_NEW_REGIONAL_T1_linear_hemi_effects_MALES.csv, and Hemi_NEW_REGIONAL_T1_linear_hemi_effects_FEMALES.csv at https://github.com/MaxKorbmacher/Hemispheric_Brain_Age.

Males

T_1 Metric	SS	F	dMRI Metric	SS	F
Hippocampus volume (rh)	316544.24	6766.75	DTI - RD fornix striaterminalis (rh)	286594.17	6364.49
Hippocampus volume (lh)	306351.25	6487.54	DTI - FA fornix striaterminalis (rh)	276467.17	6067.57
Superior temporal thickness (lh)	286384.87	5955.49	DTI - FA anterior corona radiata (lh)	274955.01	6023.83
Thickness (lh)	284626.62	5909.55	DTI - FA IFOF (lh)	263814.28	5706.24
Thickness (rh)	283428.75	5878.34	DTI - RD anterior corona radiata (lh)	246467.64	5227.51
Inferior parietal thickness (rh)	271677.80	5575.68	DTI - RD anterior corona radiata (rh)	242227.42	5113.30
Inferior lateral ventricle volume (lh)	254969.32	5156.08	DTI - FA anterior corona radiata (rh)	238605.78	5016.60
Superior temporal thickness (rh)	252923.59	5105.55	DTI - FA IFOF (rh)	233533.32	4882.47
Thalamus volume (rh)	247813.43	4980.11	BRIA - microRD ATR (rh)	232131.22	4845.66
Amygdala volume (lh)	243131.64	4866.16	DTI - RD IFOF (lh)	230505.57	4803.12

T_1 Metric	SS	F	dMRI Metric	SS	F
Superior temporal thickness (lh)	295682.20	6561.30	DTI - RD fornix striaterminalis (rh)	282234.33	6743.14
Inferior parietal thickness (rh)	288649.89	6365.48	DTI - FA anterior corona radiata (lh)	279013.72	6641.48
Thickness (lh)	287657.68	6338.05	DTI - FA IFOF (lh)	263549.29	6163.65
Thickness (rh)	274795.27	5986.72	DTI - RD anterior corona radiata (rh)	258369.12	6007.30
Superior temporal thickness (rh)	266558.45	5765.84	DTI - RD anterior corona radiata (lh)	257953.77	5994.85
Hippocampus volume (rh)	248481.56	5291.98	DTI - FA fornix striaterminalis (rh)	251128.24	5791.79
Hippocampus volume (lh)	248438.59	5290.87	BRIA - microRD ATR (rh)	249535.85	5744.86
Supramarginal thickness (rh)	232265.05	4879.14	BRIA - microRD ATR (lh)	243660.64	5573.15
Supramarginal thickness (lh)	225512.01	4710.53	DTI - FA anterior corona radiata (rh)	243324.99	5563.40
Precuneus thickness (rh)	223530.22	4661.41	DTI - RD IFOF (lh)	241625.80	5514.19

9 Description of white matter features by diffusion approaches.

Diffusion Approach	Metrics
Bayesian Rotationally Invariant Approach (BRIA) [101]	intra-axonal axial diffusivity (DAX intra) extra-axonal radial diffusivity (DRAD extra) microscopic fractional anisotropy (micro FA) extra-axonal axial diffusivity (DAX extra) intra-axonal water fraction (V intra) extra-axonal water fraction (V extra) cerebrospinal fluid fraction (vCSF) microscopical axial diffusivity (micro AX) microscopic radial diffusivity (micro RD) microscopical apparent diffusion coefficient (micro ADC)
Diffusion Kurtosis Imaging (DKI) [97, 98]	mean kurtosis (MK) radial kurtosis (RK) axial kurtosis (AK)
Diffusion Tensor Imaging (DTI) [96]	fractional anisotropy (FA) axial diffusivity (AD) mean diffusivity (MD) radial diffusivity (RD)
Spherical Mean Technique (SMT) [99]	fractional anisotropy (SMT FA) mean diffusivity (SMT md) transverse diffusion coefficient (SMT trans) longitudinal diffusion coefficient (SMT long)
Multi-compartment Spherical Mean Technique (SMTmc) [100]	extra-neurite microscopic mean diffusivity (SMTmc extra md) extra-neurite transverse microscopic diffusivity (SMTmc extra trans) mc SMTdiffusion coefficient (SMT mcd) intra-neurite volume fraction (SMTmc intra)
White Matter Tract Integrity (WMTI) [98]	axonal water fraction (AWF) radial extra-axonal diffusivity (radEAD) axial extra-axonal diffusivity (axEAD)

10 Differences of T_1w and dMRI features between hemispheres

The table shows the ten largest regional differences between left and right hemispheres' T_1w and dMRI data indicated by effect size (Cohen's d) indicated by paired samples t-tests (two-sided). SLFT = Superior longitudinal fasciculus (temporal part), ILF = Inferior longitudinal fasciculus. Bonferroni-adjusted p-values were $p < 2 \times 10^{-308}$. For full tables see the files Hemi_dMRI_features_diff.csv and Hemi_T1w_features_diff.csv at https://github.com/MaxKorbmacher/Hemispheric_Brain_Age.

T_1-weighted MRI			**diffusion MRI**		
Feature	**T-value**	**Cohen's d**	**Feature**	**T-value**	**Cohen's d**
Transverse temporal area	397.45	1.81	DTI - FA ILF	725.48	3.64
Frontal pole area	-386.34	1.76	DTI - AD SLFT	-444.89	2.23
Pars orbitalis area	-380.71	1.74	DTI - FA cingulate gyrus	388.09	1.95
Inferior parietal area	-368.85	1.68	DKI - RK cingulate gyrus	375.36	1.89
Inferior parietal volume	-352.95	1.61	SMTmc - diff SLFT	-369.19	1.85
Frontal pole volume	-340.08	1.55	SMTmc - extratrans cerebral peduncle	-367.31	1.84
Middletemporal area	-297.79	1.36	DKI - RK SLFT	-364.52	1.83
Thalamus Proper	296.93	1.35	WMTI - AWF cingulate gyrus	364.46	1.83
Transverse temporal volume	292.04	1.33	SMT - long SLFT	-359.08	1.80
Pars orbitalis volume	-280.74	1.28	DTI - AD ILF	353.43	1.78

11 Permutation feature importance for multimodal, T_1-weighted, and dMRI features between hemispheres considering *both sexes together*

Permutation feature importance shows the contribution of each feature $R^2 \pm SD$ (standard deviation) to the (brain) age predictions using multimodal, T_1-weighted, and dMRI models of each hemisphere on their own and both hemispheres together. Retroen. = Retrolenticular, l.o.int.caps. = limb of the internal capsule, cerebell.ped. = cerebellar peduncle. ATR = anterior thalamic radiation, CST = corticospinal tract, IFOF = inferior fronto-occipital fasciculus, SLF = superior longitudinal fasciculus.

Multimodal MRI					
Both hemispheres		**Left hemisphere**		**Right hemisphere**	
DKI – AK Anterior l.o.int.caps. (rh)	0.083 ± 0.0010	DTI – AK Anterior l.o.int.caps.	0.058 ± 0.0007	DKI – AK Anterior l.o.int.caps.	0.096 ± 0.0006
DTI – RD Fornix Striaterminalis (rh)	0.049 ± 0.0006	DTI – FA Superior cerebell.ped.	0.031 ± 0.0004	DTI – RD Fornix Striaterminalis	0.033 ± 0.0006
Cortex volume (lh)	0.018 ± 0.0004	Cerebellum WM volume	0.023 ± 0.0004	DTI – FA Superior cerebell.ped.	0.03 ± 0.0006
DTI – FA Cerebral peduncle (lh)	0.015 ± 0.0003	Inferior Lateral Ventricle volume	0.022 ± 0.0003	Cerebellum WM volume	0.024 ± 0.0005
DKI – AK Anterior l.o.int.caps. (lh)	0.013 ± 0.0002	Thalamus volume	0.019 ± 0.0003	Thalamus volume	0.02 ± 0.0005
DTI – FA Superior cerebell.ped. (lh)	0.011 ± 0.0002	DKI – RK Fornix-stria terminalis	0.019 ± 0.0003	BRIA – vCSF external capsule	0.018 ± 0.0004
ROI 3a area (rh)	0.01 ± 0.0002	Putamen volume	0.019 ± 0.0003	Hippocampus volume	0.017 ± 0.0004
ROI 3a area (lh)	0.01 ± 0.0002	BRIA – vCSF External capsule	0.019 ± 0.0003	Lateral ventricle volume	0.017 ± 0.0004
BRIA – vCSF External capsule (lh)	0.01 ± 0.0002	Lateral Ventricle volume	0.017 ± 0.0003	DKI – RK Posterior l.o.int.caps.	0.016 ± 0.0004
DTI – FA Superior cerebell.ped. (rh)	0.008 ± 0.0002	WMTI – AWF Superior cerebell.ped.	0.017 ± 0.0003	WMTI – AWF Retroen. l.o.int.caps.	0.014 ± 0.0004
diffusion-weighted MRI					
Both hemispheres		**Left hemisphere**		**Right hemisphere**	
DKI – AK Anterior l.o.int.caps. (rh)	0.103 ± 0.0012	DKI – AK Anterior l.o.int.caps.	0.095 ± 0.0013	DKI – AK Anterior l.o.int.caps.	0.126 ± 0.0012
DTI – RD Fornix Striaterminalis (rh)	0.061 ± 0.0009	BRIA – vCSF ATR	0.025 ± 0.0007	DTI – RD Fornix Stria terminalis	0.086 ± 0.0011
DTI – FA Cerebral peduncle (lh)	0.018 ± 0.0005	DKI – RK Fornix-stria terminalis	0.023 ± 0.0005	DTI – FA Superior cerebell.ped.	0.018 ± 0.0006
DTI – FA Anterior corona radiata (lh)	0.012 ± 0.0003	DTI – FA Fornix-stria terminalis	0.022 ± 0.0007	DKI – AK PTR	0.018 ± 0.0006
DKI – AK Anterior l.o.int.caps. (lh)	0.011 ± 0.0003	DTI – FA Cerebral peduncle	0.022 ± 0.0006	BRIA – vCSF SLF	0.017 ± 0.0006
DTI – FA Superior cerebell.ped. (lh)	0.010 ± 0.0003	DTI – FA Anterior corona radiata	0.022 ± 0.0005	DKI – AK Superio rcerebell.ped.	0.015 ± 0.0005
DTI – AD Superior l.o.int.caps. (lh)	0.010 ± 0.0003	WMTI – AWF Retroen. l.o.int.caps.	0.02 ± 0.0005	WMTI – AWF Retroen. l.o.int.caps.	0.014 ± 0.0005
DTI – AD Posterior l.o.int.caps. (lh)	0.010 ± 0.0003	DTI – FA IFOF	0.018 ± 0.0005	DTI – AD CST	0.013 ± 0.0005
DTI – AD CST (lh)	0.009 ± 0.0003	DKI – AK Superior frontooccipital fasciculus	0.017 ± 0.0006	BRIA – vCSF ATR	0.011 ± 0.0005
WMTI – AWF Retroen. l.o.int.caps. (lh)	0.009 ± 0.0002	DTI – FA Superior cerebell.ped.	0.016 ± 0.0005	DKI – RK Posterior l.o.int.caps.	0.01 ± 0.0005
T1-weighted MRI					
Both hemispheres		**Left hemisphere**		**Right hemisphere**	
Cortex volume (lh)	0.041 ± 0.0008	Lateral ventricle volume	0.071 ± 0.0011	Lateral ventricle volume	0.115 ± 0.0013
ROI PreS area (lh)	0.018 ± 0.0004	Inf.Lat.Vent volume	0.065 ± 0.0008	Inferiorparietal thickness	0.037 ± 0.0006
ROI 3a area (rh)	0.014 ± 0.0004	Superior temporal thickness	0.034 ± 0.0007	Superiortemporal thickness	0.036 ± 0.0006
Mean thickness (lh)	0.014 ± 0.0004	Insula volume	0.03 ± 0.0006	Inf.Lat.Vent volume	0.035 ± 0.0006
ROI Pol1 volume (rh)	0.013 ± 0.0005	Putamen volume	0.028 ± 0.0006	Inferior temporal area	0.029 ± 0.0006
ROI H area (lh)	0.011 ± 0.0003	Mean thickness	0.023 ± 0.0005	Thalamus volume	0.029 ± 0.0006
ROI PI thickness (lh)	0.011 ± 0.0004	Cerebellum WM volume	0.022 ± 0.0005	Cerebellum WM volume	0.028 ± 0.0005
ROI 52 area (lh)	0.011 ± 0.0003	Thalamus volume	0.02 ± 0.0005	Insula volume	0.028 ± 0.0006
ROI 3a area (lh)	0.009 ± 0.0003	Temporal pole volume	0.019 ± 0.0005	Superior frontal thickness	0.025 ± 0.0004
ROI H thickness (lh)	0.009 ± 0.0003	Amygdala volume	0.016 ± 0.0003	Hippocampus volume	0.022 ± 0.0005

12 Permutation feature importance for multimodal, T_1-weighted, and dMRI features between hemispheres considering *males only*

Permutation feature importance shows the contribution of each feature $R^2 \pm SD$ (standard deviation) to the (brain) age predictions using multimodal, T_1-weighted, and dMRI models of each hemisphere on their own and both hemispheres together. Inf.Lat.Vent. = Inferior Lateral Ventricle, retroen. = Retrolenticular, l.o. inf. int.caps = limb of the inferior internal capsule, Ant. = anterior, l.o. inf. ext.caps. = limb of the external capsule, l.o.int.caps. = limb of the internal capsule, cerebell.ped. = cerebellar peduncle, SFF = superior frontooccipital fasciculus, ATR = anterior thalamic radiation, CST = corticospinal tract, IFOF = inferior fronto-occipital fasciculus, SLF = superior longitudinal fasciculus, UF = uncinate fasciculus, PTR = Posterior thalamic radiation.

Multimodal MRI

Both hemispheres		**Left hemisphere**		**Right hemisphere**	
DKI - AK Ant. l.o. inf. int.caps (rh)	0.063 ± 0.0009	DKI – AK Ant. l.o.int.caps.	0.049 ± 0.0009	DKI – AK Ant. l.o.int.caps.	0.071 ± 0.0012
DTI - RD Fornix-Striaterminalis (rh)	0.023 ± 0.0005	DTI – FA Superior cerebell.ped.	0.025 ± 0.0007	DTI – RD Fornix Stria	0.033 ± 0.0009
Inf.Lat.Vent. volume (lh)	0.015 ± 0.0004	Inf.Lat.Vent volume	0.024 ± 0.0006	DTI – FA Superior cerebell.ped.	0.028 ± 0.0009
Putamen volume (lh)	0.010 ± 0.0002	Cerebellum WM volume	0.023 ± 0.0005	Lateral ventricle volume	0.016 ± 0.0006
Thalams volume (lh)	0.009 ± 0.0003	Thalamus volume	0.022 ± 0.0005	Thalamus volume	0.015 ± 0.0005
Thalams volume (rh)	0.009 ± 0.0003	Putamen volume	0.019 ± 0.0006	Cerebellum WM volume	0.014 ± 0.0004
Amygdala volume (lh)	0.009 ± 0.0003	WMTI – AWF Superior cerebell.ped.	0.016 ± 0.0004	Hippocampus volume	0.013 ± 0.0004
DTI - FA Superior cerebell.ped. (rh)	0.009 ± 0.0003	Lateral Ventricle	0.016 ± 0.0004	BRIA – vCSF external capsule	0.012 ± 0.0005
BRIA - vCSF External capsule (lh)	0.009 ± 0.0002	DKI – RK Fornix-stria terminalis	0.013 ± 0.0004	WMTI – AWF Superior cerebell.ped.	0.010 ± 0.0029
Cerebellum WM volume (rh)	0.009 ± 0.0002	Amygdala volume	0.012 ± 0.0005	DKI – RK Posterior l.o.int.caps.	0.010 ± 0.0029

diffusion-weighted MRI

Both hemispheres		**Left hemisphere**		**Right hemisphere**	
DKI - AK Ant. l.o. inf. ext.caps. (rh)	0.097 ± 0.0015	DKI – AK Ant. l.o.int.caps.	0.100 ± 0.0020	DKI – AK Ant. l.o.int.caps.	0.123 ± 0.0021
DTI - RD Fornix-Striaterminalis (rh)	0.061 ± 0.0013	BRIA – vCSF ATR	0.028 ± 0.0009	DTI – RD Fornix Striaterminalis	0.078 ± 0.0015
DTI - FA Cerebral peduncle (lh)	0.022 ± 0.0007	DTI – FA Cerebral peduncle	0.028 ± 0.0008	DTI – FA Superior cerebell.ped.	0.018 ± 0.0005
DTI - FA Ant. corona radiata (lh)	0.019 ± 0.0006	DTI – FA IFOF	0.027 ± 0.0008	BRIA – vCSF ATR	0.017 ± 0.0006
DKI - AK Ant. l.o. inf. ext.caps. (lh)	0.015 ± 0.0005	DTI – FA Ant. corona radiata	0.023 ± 0.0007	DTI – AD CST	0.015 ± 0.0005
DTI - FA Superior cerebell.ped. (lh)	0.012 ± 0.0004	DKI – RK Fornix-stria terminalis	0.021 ± 0.0006	DKI – AK PTR	0.013 ± 0.0004
BRIA - vextra SLF (rh)	0.011 ± 0.0004	DTI – FA Fornix-stria terminalis	0.021 ± 0.0008	WMTI – AWF retroen. int.caps.	0.012 ± 0.0004
DTI - FA IFOF (lh)	0.010 ± 0.0003	DKI – AK SFF	0.021 ± 0.0007	BRIA – vextra SLF	0.012 ± 0.0005
DKI - AK SFF (rh)	0.010 ± 0.0004	DTI – FA Superior cerebell.ped.	0.017 ± 0.0007	DKI – AK UF	0.011 ± 0.0005
BRIA - vCSF External capsule (lh)	0.009 ± 0.0002	WMTI – AWF retroen. l.o. int.caps.	0.016 ± 0.0006	DKI – AK ATR	0.011 ± 0.0003

T_1-weighted MRI

Both hemispheres		**Left hemisphere**		**Right hemisphere**	
Inf.Lat.Vent (lh)	0.051 ± 0.0011	Inf.Lat.Vent volume	0.064 ± 0.0014	Lateral ventricle volume	0.107 ± 0.002
Lateral Ventricle (rh)	0.034 ± 0.0008	Lateral Ventricle	0.049 ± 0.0011	Inf.Lat.Vent volume	0.042 ± 0.0010
Thalamus volume (rh)	0.019 ± 0.0006	Putamen volume	0.036 ± 0.0011	Hippocampus volume	0.266 ± 0.0009
Superior temporal thickness (lh)	0.019 ± 0.0006	Insula volume	0.034 ± 0.0012	Thalamus volume	0.026 ± 0.0008
Putamen volume (lh)	0.017 ± 0.0006	Temporal pole volume	0.023 ± 0.0006	Isthmus cingulate thickness	0.022 ± 0.0005
Insula volume (lh)	0.017 ± 0.0007	Superior temporal thickness	0.023 ± 0.0006	Superior temporal thickness	0.021 ± 0.0007
Hippocampus volume (rh)	0.017 ± 0.0006	Amygdala volume	0.020 ± 0.0006	Temporal pole volume	0.020 ± 0.0007
Amygdala volume (rh)	0.017 ± 0.0006	Thalamus volume	0.018 ± 0.0006	Superior frontal thickness	0.019 ± 0.0005
Inf.Lat.Ventricle (rh)	0.016 ± 0.0007	Cerebellum WM volume	0.018 ± 0.0004	Cerebellum WM volume	0.019 ± 0.0006
Temporal pole volume (rh)	0.0162 ± 0.0007	Isthmus cingulate thickness	0.014 ± 0.0004	Insula volume	0.019 ± 0.0005

13 Permutation feature importance for multimodal, T_1-weighted, and dMRI features between hemispheres considering *females only*

Permutation feature importance shows the contribution of each feature $R^2 \pm SD$ (standard deviation) to the (brain) age predictions using multimodal, T_1-weighted, and dMRI models of each hemisphere on their own and both hemispheres together. Inf.Lat.Vent. = Inferior Lateral Ventricle, retroen. = Retrolenticular, l.o. inf. int.caps = limb of the inferior internal capsule, Ant. = anterior, l.o. inf. ext.caps. = limb of the external capsule, l.o.int.caps. = limb of the internal capsule, cerebell.ped. = cerebellar peduncle, SFF = superior frontooccipital fasciculus, ATR = anterior thalamic radiation, CST = corticospinal tract, IFOF = inferior fronto-occipital fasciculus, SLF = superior longitudinal fasciculus, UF = uncinate fasciculus, PTR = Posterior thalamic radiation.

Multimodal MRI

Both hemispheres		**Left hemisphere**		**Right hemisphere**	
DKI - AK Anterior l.o. Int.caps. (rh)	0.077 ± 0.0012	DKI - AK Ant. l.o.int.caps.	0.056 ± 0.0008	DKI - AK Ant. l.o.int.caps.	0.107 ± 0.0015
DTI - RD Fornix-Striaterminalis (rh)	0.024 ± 0.0008	DTI - FA Superior cerebell.ped.	0.031 ± 0.0004	DTI - RD Fornix-striaterminalis	0.035 ± 0.0007
DTI - FA Superior cerebell. ped. (lh)	0.011 ± 0.0004	DKI - RK Fornix-Striaterminalis	0.022 ± 0.0003	DTI - FA Superior cerebell.ped.	0.034 ± 0.0006
DTI - AD Posterior l.o. ext.caps. (lh)	0.010 ± 0.0003	Cerebellum WM volume	0.022 ± 0.0003	Thalamus volume	0.020 ± 0.0004
Inferior parietal thickness (rh)	0.010 ± 0.0005	Putamen volume	0.019 ± 0.0003	Inferior parietal thickness	0.018 ± 0.0003
Thalamus volume (rh)	0.008 ± 0.0004	Lateral ventricle volume	0.019 ± 0.0003	Cerebellum WM volume	0.018 ± 0.0005
Cerebellum WM volume (rh)	0.007 ± 0.0004	DKI - AK PTR	0.017 ± 0.0003	DKI - AK PTR	0.014 ± 0.0003
DTI - FA Superior cerebell. ped. (rh)	0.007 ± 0.0003	BRIA - vCSF External capsule	0.017	Lateral ventricle volume	0.014 ± 0.0004
BRIA - vCSF External capsule (lh)	0.006 ± 0.0003	WMTI - AWF Superior cerebell.ped.	0.016 ± 0.0002	BRIA - vCSF External capsule	0.013 ± 0.0003
DTI - FA Superior cerebell. ped. (lh)	0.006 ± 0.0002	Thalamus volume	0.016 ± 0.0003	DKI - RK Posterior l.o. inf. ext.caps.	0.012 ± 0.0003

diffusion-weighted MRI

Both hemispheres		**Left hemisphere**		**Right hemisphere**	
DKI - AK Ant. l.o. inf. ext.caps. (rh)	0.129 ± 0.0019	DKI – AK Ant. l.o.int.caps.	0.101 ± 0.0016	DKI – AK Ant. l.o.int.caps.	0.160 ± 0.002
DTI - RD Fornix-Striaterminalis (rh)	0.062 ± 0.0009	DKI – RK Fornix-stria terminalis	0.037 ± 0.0006	DTI – RD Fornix Striaterminalis	0.099 ± 0.0011
DTI - FA Cerebral peduncle (lh)	0.022 ± 0.0004	DTI – FA Superior cerebell.ped.	0.036 ± 0.0005	DKI – AK PTR	0.030 ± 0.0003
DTI - FA Superior cerebell.ped. (lh)	0.017 ± 0.0003	DTI – FA Cerebral peduncle	0.034 ± 0.0006	DTI – FA Superior cerebell.ped.	0.026 ± 0.0003
DTI - AD Posterior l.o. inf. ext.caps. (lh)	0.015 ± 0.0002	BRIA – vCSF ATR	0.027 ± 0.0005	BRIA – vCSF ATR	0.020 ± 0.0004
DKI - AK Ant. l.o. inf. ext.caps. (lh)	0.015 ± 0.0002	DTI – RD Fornix Striaterminalis	0.025 ± 0.0006	DTI – AD CST	0.020 ± 0.0003
DKI - RK Fornix-Striaterminalis (lh)	0.013 ± 0.0003	DKI – AK PTR	0.025 ± 0.0004	DKI – AK SFF	0.020 ± 0.0003
DKI - AK SFF (lh)	0.012 ± 0.0002	DTI – FA IFOF	0.025 ± 0.0004	DKI – AK Ant. corona radiata	0.015 ± 0.0002
DTI - FA IFOF (lh)	0.011 ± 0.0002	WMTI – AWF retroen. l.o. int.caps.	0.023 ± 0.0004	DTI – AD Posterior l.o. int.caps.	0.015 ± 0.0002
DKI - AK PTR (rh)	0.011 ± 0.0002	DKI – AK SFF	0.023 ± 0.0005	BRIA – vCSF SLF	0.013 ± 0.0002

T_1-weighted MRI

Both hemispheres		**Left hemisphere**		**Right hemisphere**	
Inferiorparietal thickness (rh)	0.030 ± 0.0007	Lateral ventricle volume	0.063 ± 0.0008	Lateral ventricle volume	0.097 ± 0.0015
Lateral Ventricle (rh)	0.030 ± 0.0006	Inf.Lat.Vent volume	0.042 ± 0.0009	Inferior parietal thickness	0.044 ± 0.0008
Inf.Lat.Ventricle (lh)	0.026 ± 0.0007	Superior temporal thickness	0.037 ± 0.0011	Superior temporal thickness	0.039 ± 0.0008
Superior temporal thickness (lh)	0.024 ± 0.0007	Putamen volume	0.029 ± 0.0007	Thalamus volume	0.030 ± 0.0008
Putamen volume (lh)	0.020 ± 0.0005	Insula volume	0.029 ± 0.0006	Cerebellum WM volume	0.028 ± 0.0008
Cerebellum WM (rh)	0.017 ± 0.0006	Thalamus volume	0.026 ± 0.0006	Insula volume	0.025 ± 0.0006
Thalamus volume (rh)	0.011 ± 0.0004	Cerebellum WM volume	0.023 ± 0.0007	Inf.Lat.Vent volume	0.021 ± 0.0007
Thalamus volume (lh)	0.011 ± 0.0004	Mean thickness	0.020 ± 0.0005	Inferior temporal area	0.019 ± 0.0004
Superior temporal thickness (rh)	0.011 ± 0.0004	Amygdala volume	0.019 ± 0.0005	Superior temporal thickness	0.018 ± 0.0004
Accumbens area (lh)	0.011 ± 0.0003	Accumbens volume	0.019 ± 0.0005	Temporal pole volume	0.015 ± 0.0005

14 Sex stratified brain age model performance

R^2 = Variance explained, MAE = Mean Absolute Error, RMSE = Root Mean Squared Error, Corr. = Correlation, Values in round parentheses () refer to standard deviations and square brackets [] to 95% confidence interval around correlations (Pearson's r) of uncorrected brain age estimates and chronological age.
The correlation between raw brain age and chronological age.

Males					
Model	**Features**	**R^2**	**MAE**	**RMSE**	**Correlation***
Left T_1w	117	0.513 (0.013)	4.398 (0.059)	5.472 (0.087)	0.719 [0.712, 0.725]
Right T_1w	117	0.506 (0.012)	4.437 (0.069)	5.521 (0.101)	0.711 [0.704, 0.717]
T_1w	234	0.534 (0.010)	4.294 (0.070)	5.356 (0.096)	0.722 [0.716, 0.728]
Left dMRI	840	0.573 (0.017)	4.104 (0.077)	5.111 (0.112)	0.761 [0.755, 0.767]
Right dMRI	840	0.586 (0.015)	4.039 (0.063)	5.039 (0.108)	0.767 [0.761, 0.773]
dMRI	1680	0.608 (0.015)	3.922 (0.078)	4.908 (0.108)	0.782 [0.776, 0.787]
Left multimodal	957	0.626 (0.012)	3.794 (0.030)	4.767 (0.037)	0.795 [0.790, 0.801]
Right multimodal	957	0.630 (0.015)	3.783 (0.066)	4.743 (0.075)	0.798 [0.792, 0.803]
Multimodal	1914	0.653 (0.014)	3.688 (0.064)	4.627 (0.040)	0.808 [0.803, 0.813]
Females					
Model	**Features**	**R^2**	**MAE**	**RMSE**	**Correlation***
Left T_1w	117	0.482 (0.015)	4.424 (0.053)	5.499 (0.060)	0.696 [0.690, 0.703]
Right T_1w	117	0.470 (0.017)	4.486 (0.07)	5.570 (0.082)	0.688 [0.681, 0.694]
T_1w	234	0.504 (0.015)	4.339 (0.073)	5.403 (0.079)	0.710 [0.704, 0.716]
Left dMRI	840	0.560 (0.014)	4.043 (0.072)	4.993 (0.072)	0.745 [0.739, 0.751]
Right dMRI	840	0.573 (0.014)	3.961 (0.065)	4.925 (0.061)	0.757 [0.751, 0.763]
dMRI	1680	0.597 (0.013)	3.845 (0.069)	4.815 (0.058)	0.773 [0.767, 0.778]
Left multimodal	957	0.608 (0.016)	3.782 (0.016)	4.696 (0.094)	0.778 [0.773, 0.784]
Right multimodal	957	0.613 (0.016)	3.746 (0.095)	4.664 (0.098)	0.785 [0.780, 0.790]
Multimodal	1914	0.633 (0.017)	3.653 (0.085)	4.577 (0.080)	0.798 [0.793, 0.803]

15 Tuned hyperparameters for sex stratified brain age models

Overview of the tuned hyperparameters for each of the sex-specific brain age models.

Males

Modality	Hemisphere	Learning Rate	Maximum Depth	Number of Trees
Multimodal	Both	0.1	6	140
Multimodal	Left	0.1	5	140
Multimodal	Right	0.1	4	180
dMRI	Both	0.1	5	140
dMRI	Left	0.1	4	180
dMRI	Right	0.05	5	180
T_1w	Both	0.1	5	60
T_1w	Left	0.1	4	180
T_1w	Right	0.1	4	180

Females

Modality	Hemisphere	Learning Rate	Maximum Depth	Number of Trees
Multimodal	Both	0.1	4	180
Multimodal	Left	0.05	8	180
Multimodal	Right	0.05	6	180
dMRI	Both	0.05	7	180
dMRI	Left	0.05	7	140
dMRI	Right	0.05	8	180
T_1w	Both	0.1	5	140
T_1w	Left	0.05	6	180
T_1w	Right	0.1	5	180

SUPPLEMENTARY FIGURES

1 Uncorrected mean values' age curves

Uncorrected standardized and zero-centered age curves and lines for mean values of grey and white and grey matter features by age per hemisphere. For line fitting, first, a cubic smooth function (s) with $k = 4$ knots was applied to plot the relationship between age and brain features (F): $\hat{age} = s(F)$. Second, a linear model was applied of the following form: $\hat{age} = \beta_0 + \beta_1 \times F$. Models used restricted maximum likelihood (REML). Extreme outliers defined by Mean±9SD were removed for visualisation purposes.

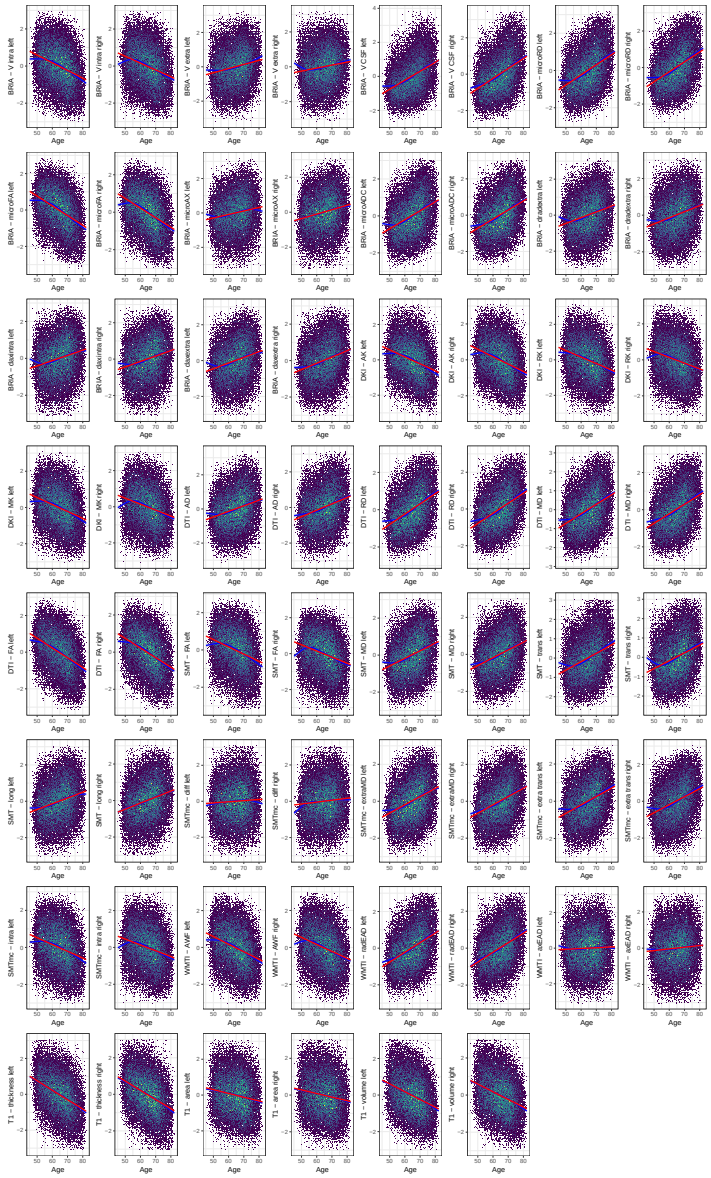

2 Distribution of the *significant and non-significant* slopes of age-related laterality indexed grey and white matter features

We estimated the absolute laterality index ($|LI|$) for each regional feature to assess the overall directionality of asymmetry-age associations. The distrubutions of age-relationship of $|LI|$ are displayed with the six panels showing the distributions for the modality-specific features (T_1-weighted and diffusion-weighted) for both sexes, males and females.

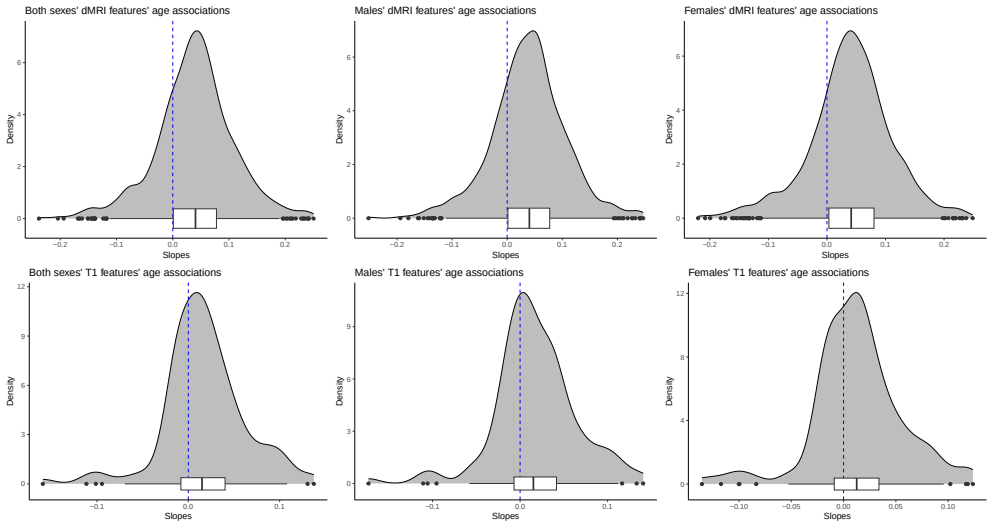

3 Distribution of the *significant* slopes of age-related laterality indexed grey and white matter features

We estimated the absolute laterality index ($|LI|$) for each regional feature to assess the overall directionality of asymmetry-age associations. The distrubutions of age-relationship of $|LI|$ are displayed with the six panels showing the distributions for the modality-specific features (T_1-weighted and diffusion-weighted) for both sexes, males and females.

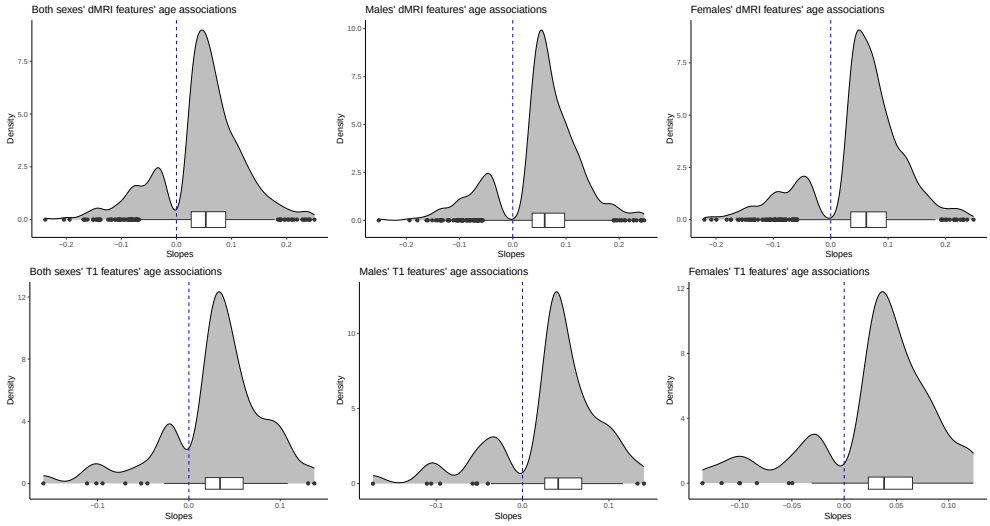

4 Linear, adjusted hemispheric mean values' age associations

Corrected standardized and zero-centered linear age relationships for mean hemispheric values of grey and white matter features by age per hemisphere. Modelling was done using Eq. 2: $a\hat{g}e = \beta_0 + \beta_1 \times F + \beta_2 \times Sex + \beta_3 \times Site$, where F is the respective brain feature.

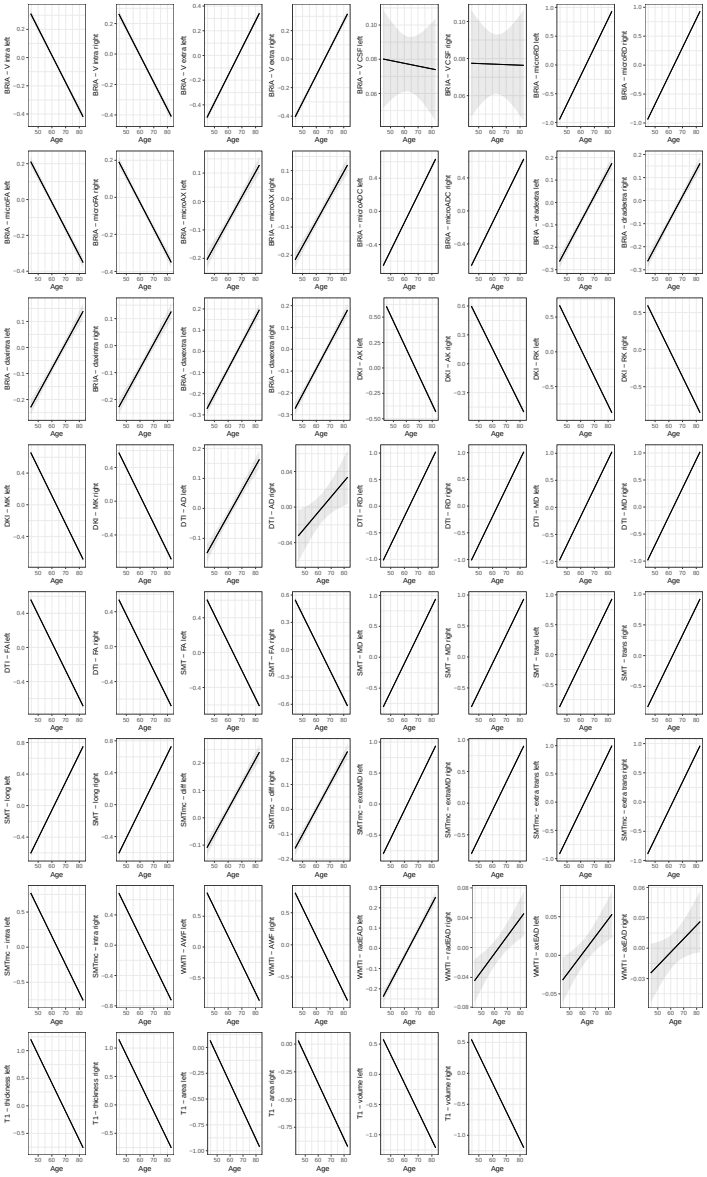

5 Adjusted mean values' hemisphere-specific age associations by sex

Age curves of standardized and zero-centered mean values of GM and WM features per hemisphere and by sex. A cubic smooth function (s) with $k = 4$ knots was applied to plot the relationship between age and brain features correcting for sex and scanner site (F): $\hat{age} = s(F) + sex + site$ using restricted maximum likelihood (REML). The grey shaded area indicates the 95% CI. All age-relationships were significant ($p_{adj} < .05$).

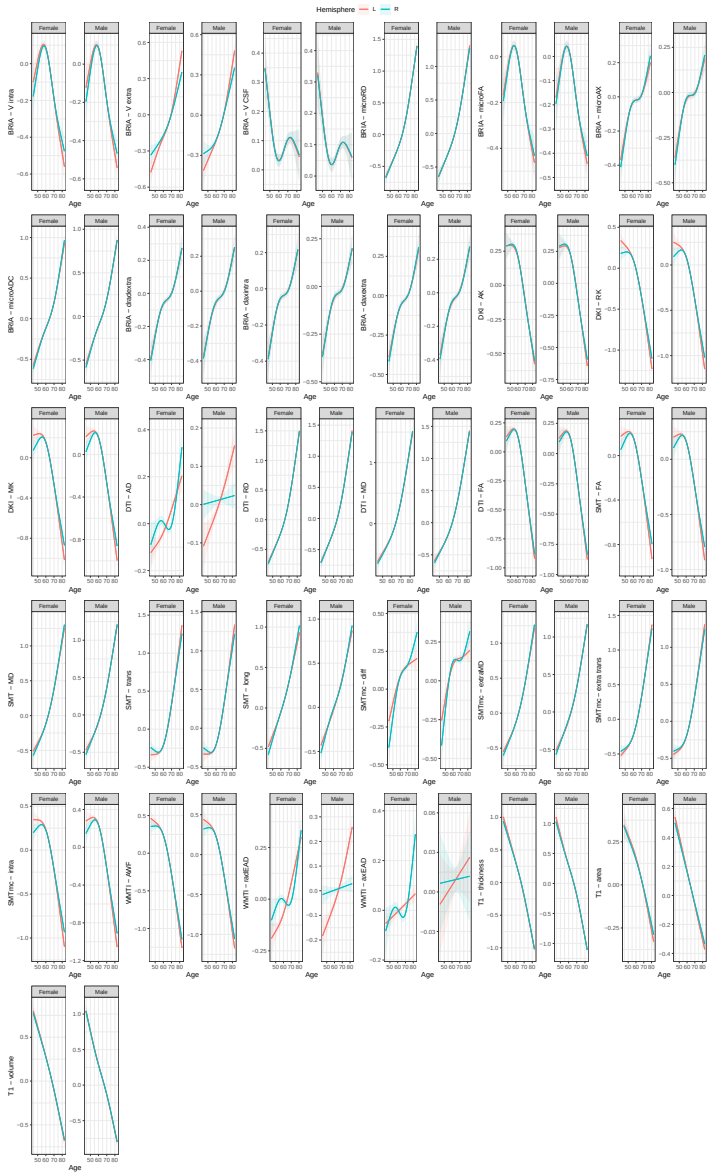

6 Adjusted mean values' sex-specific age associations by hemisphere

Age curves of standardized and zero-centered mean values of GM and WM features per hemisphere and by sex. A cubic smooth function (s) with $k = 4$ knots was applied to plot the relationship between age and brain features correcting for sex and scanner site (F): $a\hat{g}e = s(F) + sex + site$ using restricted maximum likelihood (REML). The grey shaded area indicates the 95% CI. All age-relationships were significant ($p_{adj} < .05$).

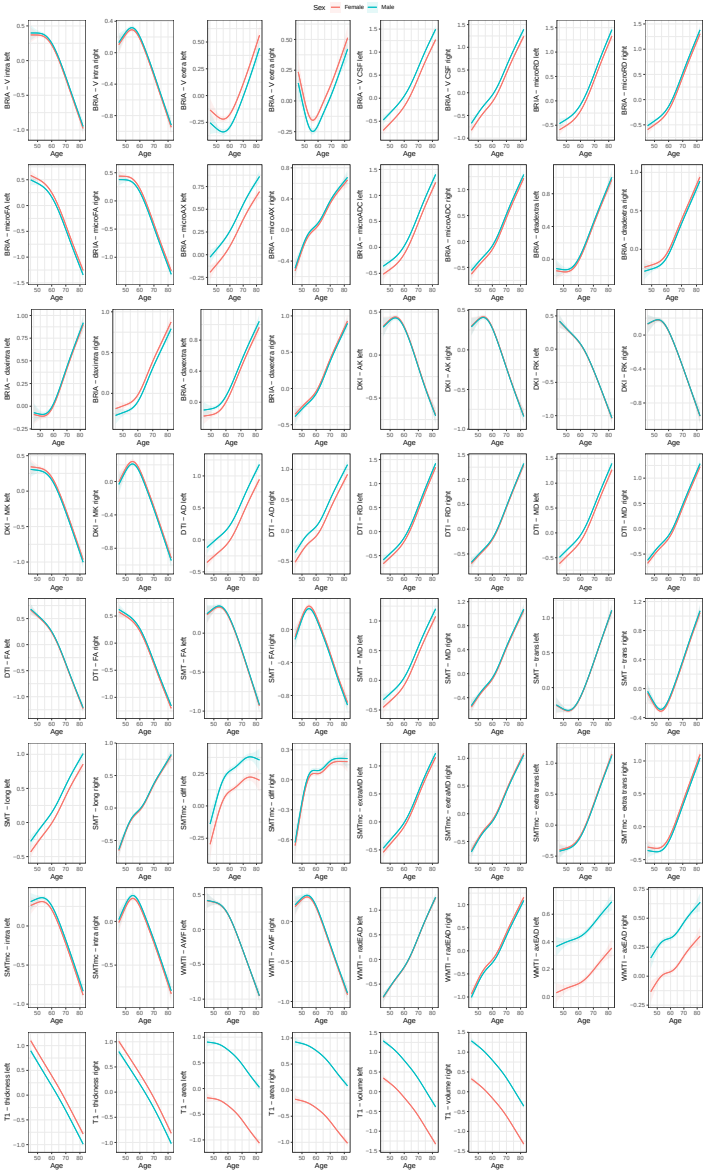

7 Association between general health-and-lifestyle phenotypes and brain age estimated from different modalities, left, right and both hemispheres by sex

Eq. 9 was used (yet stratifying by sex) and standardized slopes are presented. For simplicity, standardized slopes with $|\beta| < 0.005$ were rounded down to $\beta = 0$. Panel a) males, panel b) females. L: left hemisphere, R: right hemisphere, LR: both hemispheres, BMI: body mass index, WHR: waist-to-hip ratio. Bonferroni-adjusted $p < .05$ is marked by a black frame.

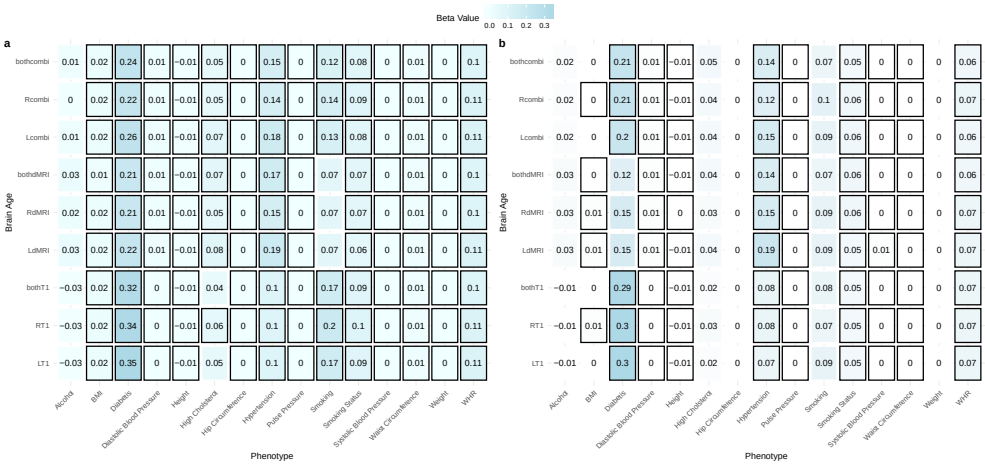

8 Males' T_1-weighted and dMRI features asymmetry-age-associations

T_1-weighted and dMRI features linear asymmetry-age-associations. The plot presents the standardized, site-corrected regression slopes versus Bonferroni-adjusted -log10 p-values for males. Modelling was done using a sex-stratified version of Eq. 2: $\hat{age} = \beta_0 + \beta_1 \times F + \beta_2 \times Site$, where F is the respective brain feature. Labelling was done separately for T_1-weighted and dMRI indicating the 10 most significantly associated features (five for $\beta > 0$ and five for $\beta < 0$). Cereb.Peduncle = cerebral peduncle, Rostro-mid. thicknes = rostro-middle thickness, SLFT = superior longitudinal fasciculus (temporal part), Fornix-Str.Term. = fornix-stria terminalis tract, Rost. ant. cingulate = rostral anterior cingulate. Full tables are available at https://github.com/MaxKorbmacher/Hemispheric_Brain_Age/.

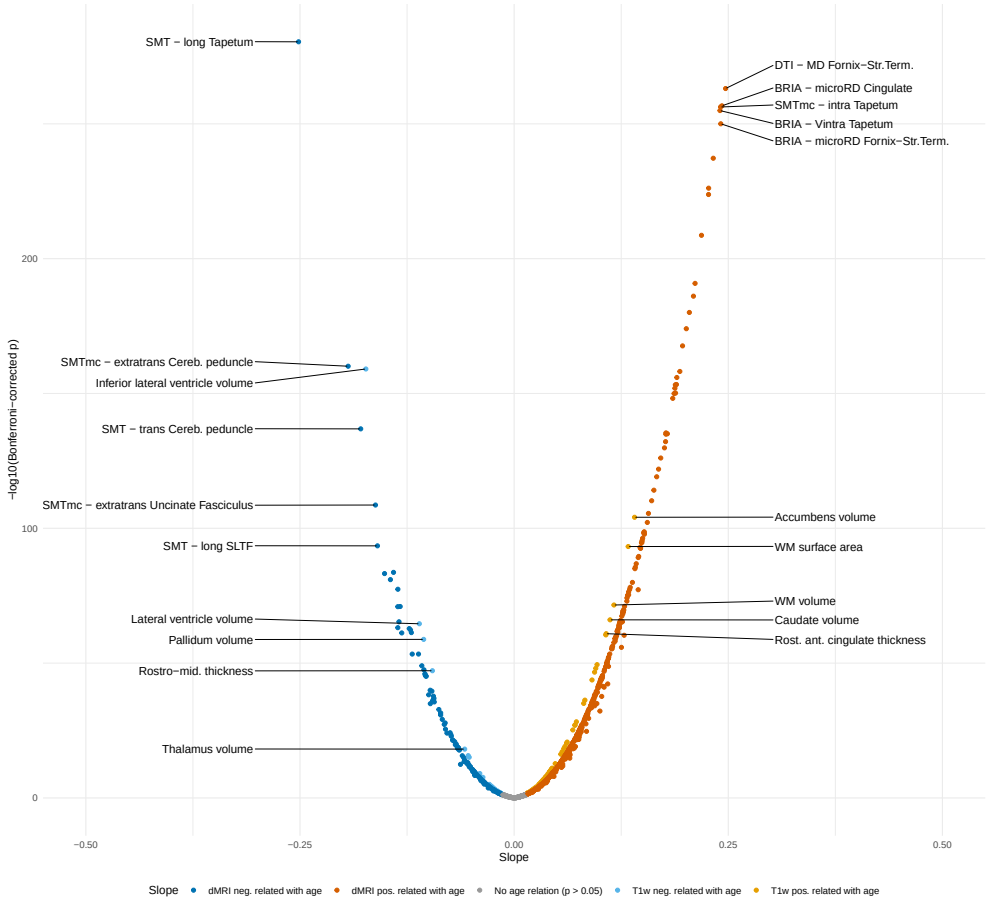

9 Females' T_1-weighted and dMRI features asymmetry-age-associations

T_1-weighted and dMRI features linear asymmetry-age-associations. The plot presents the standardized, site-corrected regression slopes versus Bonferroni-adjusted -log10 p-values for females. Modelling was done using a sex-stratified version of Eq. 2: $\hat{age} = \beta_0 + \beta_1 \times F + \beta_2 \times Site$, where F is the respective brain feature. Labelling was done separately for T_1-weighted and dMRI indicating the 10 most significantly associated features (five for $\beta > 0$ and five for $\beta < 0$). Cereb.Peduncle = cerebral peduncle, Rostro-mid. thicknes = rostro-middle thickness, SLFL = superior longitudinal fasciculus, Sup.front.occ.Fasc. = superior fronto-occipital fasciculus. Full tables are available at https://github.com/MaxKorbmacher/Hemispheric_Brain_Age/.

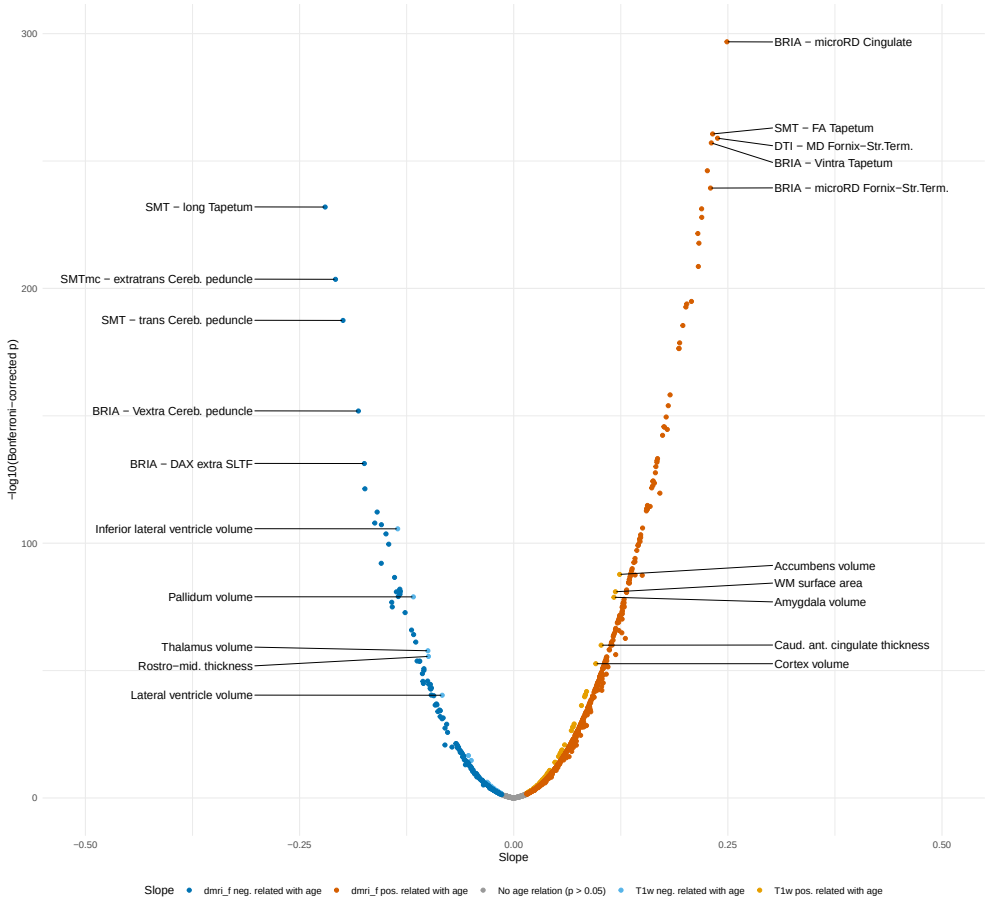

10 Pearson correlation coefficients between chronological and predicted ages for T_1-weighted, diffusion, and multimodal MRI for left, right and both hemispheres for sex stratified brain age models

All Bonferroni-corrected $p < .001$. L: left hemisphere, R: right hemisphere, LR: both hemispheres.

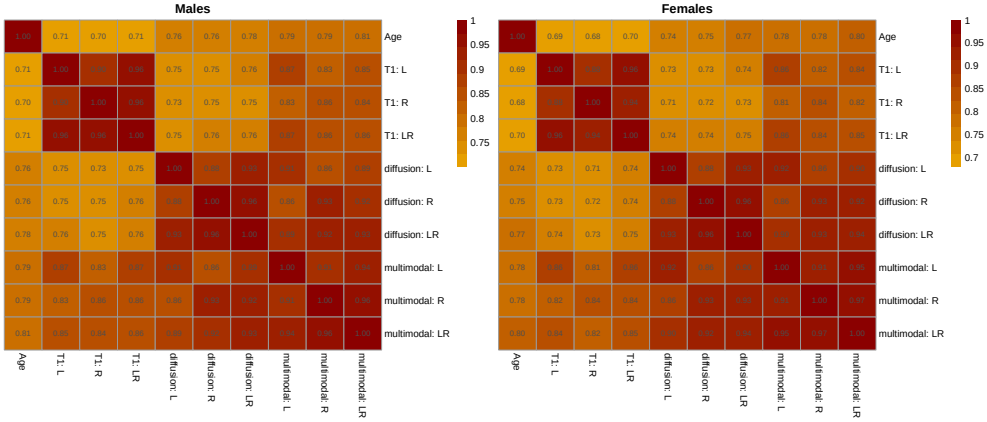

11 Association between general health-and-lifestyle phenotypes and sex-specific trained brain age estimated from different modalities, left, right and both hemispheres

Eq. 9 was used (yet stratifying by sex) and standardized slopes are presented. For brain age prediction, we used models which were trained separately for males and females, respectively. For simplicity, standardized slopes with $|\beta| < 0.005$ were rounded down to $\beta = 0$. L: left hemisphere, R: right hemisphere, LR: both hemispheres, BMI: body mass index, WHR: waist-to-hip ratio. Bonferroni-adjusted $p < .05$ is marked by a black frame.

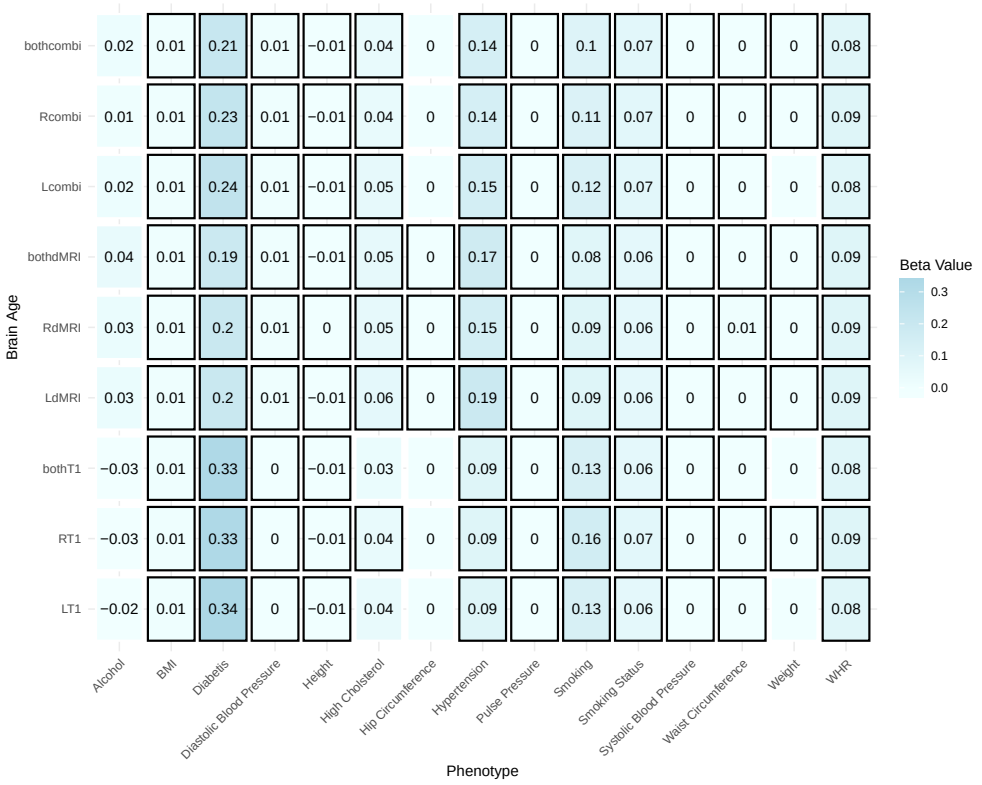

12 Association between general health-and-lifestyle phenotypes and sex-specific trained brain age estimated from different modalities, left, right and both hemispheres by sex

Eq. 9 was used (yet stratifying by sex) and standardized slopes are presented. For brain age prediction, we used models which were trained separately for males and females, respectively. For simplicity, standardized slopes with $|\beta| < 0.005$ were rounded down to $\beta = 0$. Panel a) males, panel b) females. L: left hemisphere, R: right hemisphere, LR: both hemispheres, BMI: body mass index, WHR: waist-to-hip ratio. Bonferroni-adjusted $p < .05$ is marked by a black frame.